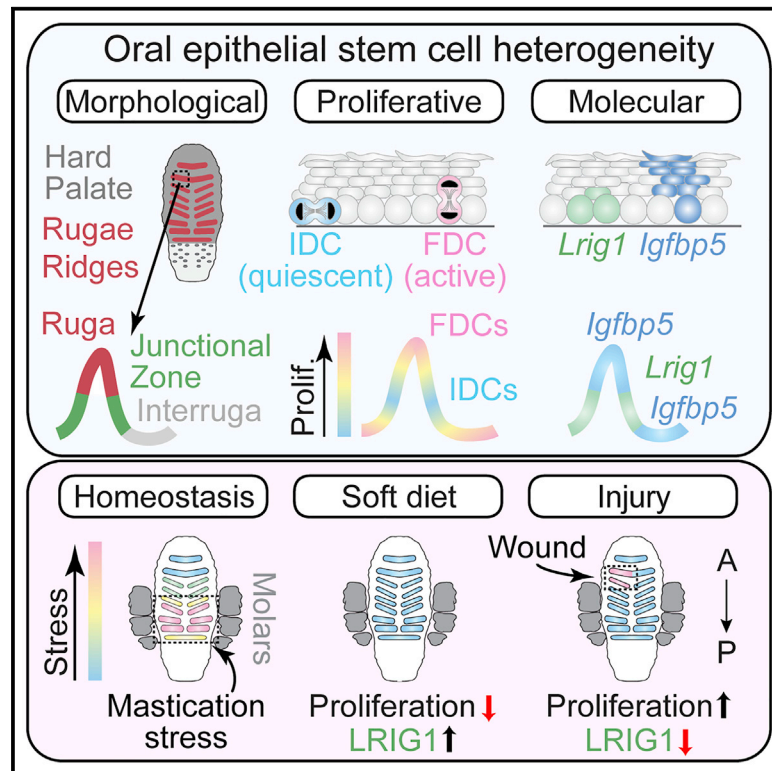


Cell Stem Cell

Heterogeneity within Stratified Epithelial Stem Cell Populations Maintains the Oral Mucosa in Response to Physiological Stress

Graphical Abstract



Authors

Kevin M. Byrd, Natalie C. Piehl, Jeet H. Patel, ..., Ophir D. Klein, Robert J. Coffey, Scott E. Williams

Correspondence

scott_williams@med.unc.edu

In Brief

Byrd et al. show that stratified epithelia of the oral cavity display unusual proliferative heterogeneity, particularly in the hard palate region. A slow-cycling population residing in the junctional zone niche is LRIG1^{HI}, self-renews through planar symmetric divisions, responds to masticatory stress, and promotes wound healing.

Highlights

- Oral epithelia are maintained by both delamination and oriented cell divisions
- The hard palate contains a slow-cycling population residing in the junctional zone
- Lrig1+ clones are biased to self-renew and Igfbp5+ clones to differentiate
- Lrig1+ slow-cycling junctional zone stem cells are stress responsive



Heterogeneity within Stratified Epithelial Stem Cell Populations Maintains the Oral Mucosa in Response to Physiological Stress

Kevin M. Byrd,^{1,2} Natalie C. Piehl,¹ Jeet H. Patel,¹ Won Jae Huh,³ Inês Sequeira,⁴ Kendall J. Lough,¹ Bethany L. Wagner,¹ Pauline Marangoni,⁵ Fiona M. Watt,⁴ Ophir D. Klein,⁵ Robert J. Coffey,^{3,6,7} and Scott E. Williams^{1,8,9,*}

¹Department of Pathology & Laboratory Medicine, the University of North Carolina School of Medicine, Chapel Hill, NC 27599, USA

²Division of Oral & Craniofacial Health Sciences, the University of North Carolina Adams School of Dentistry, Chapel Hill, NC 27599, USA

³Department of Pathology, Microbiology and Immunology, Vanderbilt University Medical Center, Nashville, TN 37232, USA

⁴Centre for Stem Cells & Regenerative Medicine, King's College London, London E1 9RT, UK

⁵Department of Pediatrics and Institute for Human Genetics, Program in Craniofacial Biology and Department of Orofacial Sciences, University of California, San Francisco, San Francisco, CA 94143, USA

⁶Cell and Developmental Biology, Vanderbilt University, Nashville, TN 37235, USA

⁷Department of Veterans Affairs Medical Center, Nashville, Vanderbilt University, TN 37212, USA

⁸Lineberger Comprehensive Cancer Center, the University of North Carolina at Chapel Hill, Chapel Hill, NC 27599, USA

⁹Lead Contact

*Correspondence: scott_williams@med.unc.edu

<https://doi.org/10.1016/j.stem.2019.11.005>

SUMMARY

Stem cells in stratified epithelia are generally believed to adhere to a non-hierarchical single-progenitor model. Using lineage tracing and genetic label-retention assays, we show that the hard palatal epithelium of the oral cavity is unique in displaying marked proliferative heterogeneity. We identify a previously uncharacterized, infrequently-dividing stem cell population that resides within a candidate niche, the junctional zone (JZ). JZ stem cells tend to self-renew by planar symmetric divisions, respond to masticatory stresses, and promote wound healing, whereas frequently-dividing cells reside outside the JZ, preferentially renew through perpendicular asymmetric divisions, and are less responsive to injury. LRIG1 is enriched in the infrequently-dividing population in homeostasis, dynamically changes expression in response to tissue stresses, and promotes quiescence, whereas Igfbp5 preferentially labels a rapidly-growing, differentiation-prone population. These studies establish the oral mucosa as an important model system to study epithelial stem cell populations and how they respond to tissue stresses.

INTRODUCTION

Epithelial stem cells must balance differentiation and self-renewal to build new tissues during development, maintain homeostasis, and repair after injury, and disequilibrium might result in stem cell depletion or cancer (Arwert et al., 2012; Hsu et al., 2014). Oral epithelia comprise highly proliferative, stratified squamous mucosa specialized for the varied functions of

feeding, speech, barrier function, breathing, and early digestion. Oral epithelial stem cells (OESCs) reside within the proliferative basal layer, while differentiating cells populate suprabasal (SB) layers (Papagerakis et al., 2014), although a recent study revealed a differentiation gradient among basal layer cells (Jones et al., 2018). Understanding how this spectrum of stem-like to transit-amplifying states is regulated might shed light on why oral mucosa heal rapidly and with minimal scarring, even in the face of constant challenges from mastication and pathogen exposure (Iglesias-Bartolome et al., 2018; Jones and Klein, 2013).

In adult epidermis, differentiation occurs primarily via delamination, or detachment, of basal cells from the underlying basement membrane (Blanpain and Fuchs, 2009). However, particularly during development, both oral epithelial and epidermal basal cells can position their mitotic spindles perpendicular to the basement membrane to execute asymmetric cell divisions (ACDs), whereby the suprabasal daughter differentiates while the basal daughter continues to proliferate. Alternatively, basal cells can execute self-renewing symmetric cell divisions (SCDs) when they divide within the epithelial plane (Byrd et al., 2016; Lechler and Fuchs, 2005; Williams et al., 2011; Williams et al., 2014). However, in adult epidermis, planar divisions can be either symmetric or operationally asymmetric, when one basal daughter delaminates after mitosis (Clayton et al., 2007; Rompolas et al., 2016). Collectively, these and other studies report that nearly all divisions in adult stratified epithelia are planar (Ichijo et al., 2017; Ipponjima et al., 2016; Jones et al., 2019; Mesa et al., 2018), suggesting that perpendicular ACDs might be a developmental adaptation to promote rapid stratification.

The epidermis was originally proposed to consist of homogeneous clones—each containing a single, asymmetrically dividing stem cell surrounded by transit-amplifying cells—forming ordered columns called epidermal proliferative units (Potten, 1974). More recently, this “invariant asymmetry” model has been opposed by a “population asymmetry” model. Genetic



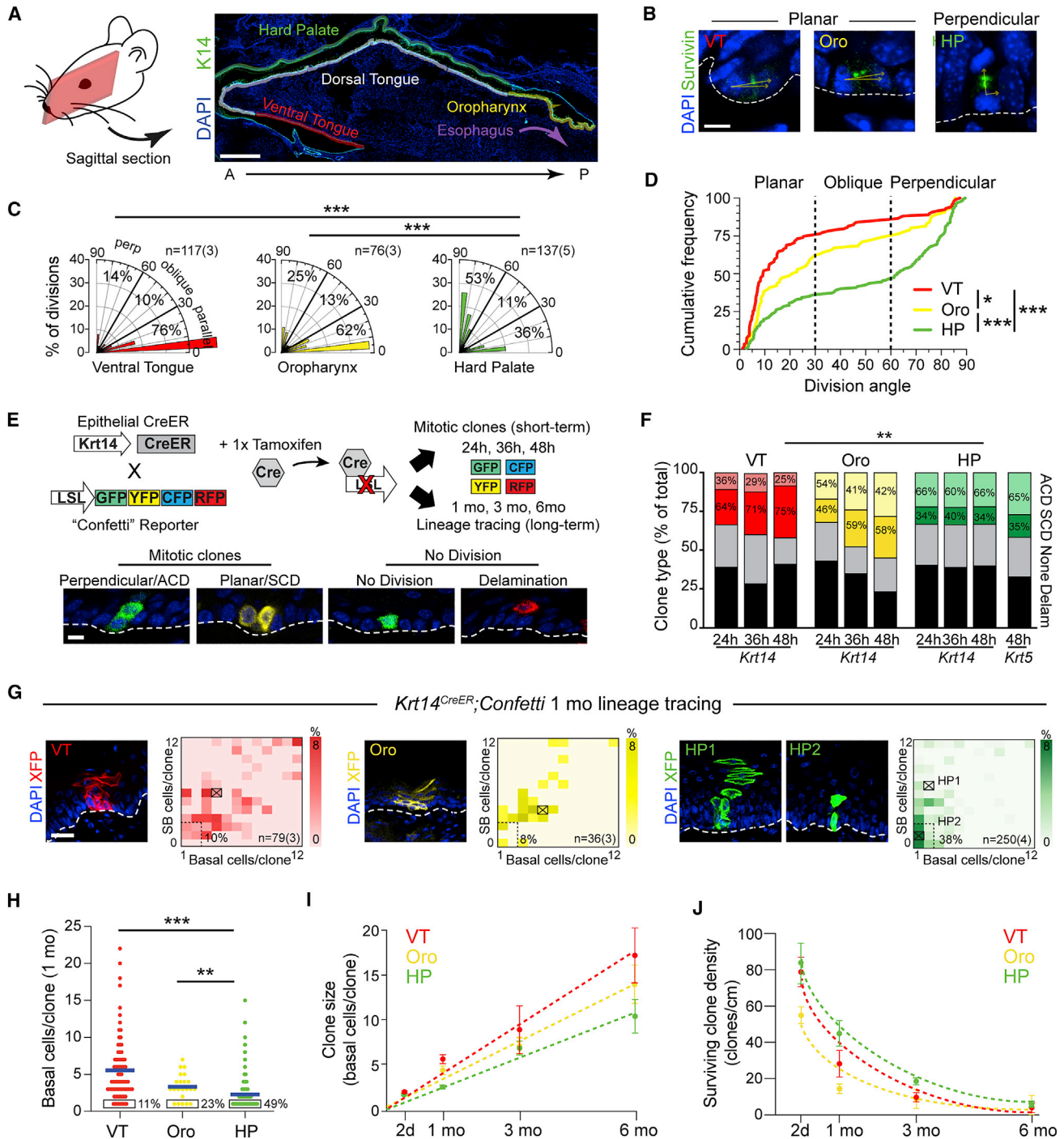


Figure 1. Palatal Epithelium Displays Unique Renewal Properties

(A) Sagittal section of adult oral cavity.
 (B) High-magnification images of late-stage mitotic cells in ventral tongue (VT), oropharynx (Oro), and hard palate (HP) used to characterize division orientation. Angles (yellow) were calculated relative to basement membrane (dashed line).
 (C and D) Division orientation by region, displayed as radial histograms (C) and cumulative frequency plots (D).
 (E and F) Overview (E) of short-term and long-term lineage-tracing strategies, with examples of the four different clonal patterns observed, quantified in (F).
 (G) 1 month *Krt14*^{CreER} lineage tracing showing representative clones (left) indicated by X's in clonal density arrays (CDAs; right). The bounding box defines slow-growing latent clones, defined as containing ≤ 2 basal and suprabasal (SB) cells; the percentage of total clones that are latent is indicated. HP1 represents a SB-rich clone; HP2 represents a latent clone.
 (H) Basal cells/clone for each region, quantified as dot plots. The percentage of total clones with one basal cell is indicated by the boxed region; blue bars indicate means.

(legend continued on next page)

lineage tracing and quantitative modeling have suggested that a single population of committed progenitors makes stochastic decisions to either self-renew or to differentiate (Clayton et al., 2007; Doupé et al., 2012; Jones et al., 2007; Klein and Simons, 2011). This leads to a phenomenon known as “neutral drift,” which makes several predictions of how clones evolve over time: (1) the number of stem cells per clone increases linearly, (2) clone sizes demonstrate “scaling” behavior, and (3) surviving clone fractions decrease in inverse proportion to the stem cell replacement rate (Klein and Simons, 2011). However, this single progenitor model has been challenged by evidence that both proliferative, committed progenitor and more quiescent stem cell populations exist in the epidermis (Mascré et al., 2012; Sada et al., 2016).

Proliferative heterogeneity among OESCs was suggested by pulse-chase studies that showed that label-retaining cells (LRCs) exist in the gingiva, tongue papillae, and palate (Asaka et al., 2009; Bickenbach, 1981; Bickenbach and Mackenzie, 1984; Willberg et al., 2006). However, a recent study utilizing lineage tracing and genetic label retention demonstrated that buccal epithelia adhere to a neutral drift model (Jones et al., 2019). Thus, whether regional OESC subpopulations exist, which markers define them, and whether they adhere to a single progenitor model remain largely unknown.

The leucine-rich repeats and immunoglobulin-like domains (Lrig) family of transmembrane proteins has emerged as key regulators of stem cell behavior due to their function in growth factor receptor regulation (Gur et al., 2004; Laederich et al., 2004). Lrig1 has been reported to label quiescent epithelial populations in the small intestine, stomach, hair follicle infundibulum, and labial cervical loop of the incisors (Choi et al., 2018; Jensen et al., 2009; Jensen and Watt, 2006; Page et al., 2013; Powell et al., 2012; Seidel et al., 2017). *Lrig1*^{-/-} mice display regional epidermal hyperplasia, supporting the idea that Lrig1 negatively regulates proliferation (Suzuki et al., 2002). Lrig1 and other family members are expressed in the oral cavity (Jones et al., 2019), but little is known about their function.

Here, using lineage tracing, genetic label retention, and functional assays, we report striking OESC proliferative heterogeneity and provide evidence for the existence of a candidate niche within the junctional zone (JZ) of the hard palate (HP). We show that JZ OESCs display characteristics of stemness, including quiescence, self-renewal through planar oriented cell divisions, and *Lrig1* enrichment. We demonstrate that OESCs are sensitive to both masticatory and wounding stresses, which impact tissue cycling/proliferation as well as *Lrig1* expression. Finally, using RNA-seq and confirmatory lineage tracing, we identify two markers of HP heterogeneity. *Lrig1* marks small, basal-rich JZ clones, whereas *Igfbp5* labels large, suprabasal-rich clones located outside the JZ. Collectively, these data support the existence of regional OESC heterogeneity and provide early clues of niche-specific regulatory mechanisms.

RESULTS

The Hard Palate Displays Unique Patterns of Oriented Cell Divisions

During stratified epithelial development, basal progenitors execute a bimodal pattern of planar SCDs and perpendicular ACDs to balance self-renewal and differentiation (Byrd et al., 2016; Lu and Johnston, 2013; Morin and Bellaïche, 2011; Seldin and Macara, 2017; Williams et al., 2011; Williams et al., 2014). However, because virtually all divisions are reported to be planar in adult stratified epithelia, differentiation might be driven by delamination rather than ACDs. To explore whether patterns of division orientation vary across oral epithelia, we investigated three different tissues: (1) ventral tongue (VT), an ectodermal-derived mucosal epithelium; (2) hard palate (HP), an ectodermal-derived masticatory epithelium, and (3) oropharynx, an endodermal-derived mucosal epithelium (Figure 1A). Despite their differences in location and morphology, proliferation rates were similar among these tissues (Figures S1A and S1B). To characterize division orientation, we used Survivin (Figure 1B), which localizes to the cleavage furrow during telophase, when division axis commitment occurs (Williams et al., 2011). Although all oral epithelia display a mix of planar and perpendicular divisions during development (Byrd et al., 2016), the majority of divisions in adult VT and oropharynx were planar. However, in HP, a bimodal distribution of perpendicular and planar divisions was observed (Figures 1C and 1D), making it the only adult stratified epithelium described where the majority of cell divisions (53%, $n = 137$) remain perpendicular.

Short-Term Lineage Tracing Reveals Regional Patterns of Renewal

To determine the relative contributions of ACDs, SCDs, and delamination to differentiation during OE homeostasis, we performed short-term (24 h, 36 h, and 48 h) lineage tracing by using a tamoxifen-inducible, basal-layer-specific *Krt14*^{CreER} transgenic crossed to a multi-fluorophore reporter (*LSL-Confetti*). We assumed that: (1) two-cell clones consisting of one basal and one SB cell divided by perpendicular ACD, (2) two-basal cell clones divided by planar SCD, (3) single-basal cell clones had not divided, and (4) single-SB clones differentiated by delamination (Figure 1E). Confirming that they have similar overall proliferation rates, the fraction of clones that divided during a 24 h labeling period was similar for all tissues (35% for HP; 34.6% for oropharynx; and 38% for VT), although the HP showed a lower incidence of larger clones, particularly at 48 h (Figures 1F and S1C). Because ~1/3 of all clones across tissues were single SB cells (Figure 1F), delamination is a significant driver of differentiation in oral epithelia. In agreement with the high proportion of planar divisions observed in VT and oropharynx, SCD clones outnumbered ACD clones in these tissues, whereas ACDs were more numerous than SCDs in HP, a result independently confirmed with a second *K5*^{CreER} reporter line (Figure 1F). The strong correlation between division angles

(I and J) Clone size (I) and clonal density (J) over time; HP clones grow most slowly and have the lowest extinction rates.

* $p < 0.05$, ** $p < 0.01$, and *** $p < 0.0001$, by χ^2 (C and F), Kolmogorov-Smirnov test (D), or Mann-Whitney test (H). Data in (I and J) are mean \pm SEM. ACD = asymmetric cell division and SCD = symmetric cell division. Scale bars: 500 μm (A), 25 μm (G), 10 μm (B and E); n values in (B and G) indicate cells and (animals/biological replicates); in (F and H–J), $n = 3$ –5 animals per group per time point. See also Figure S1.

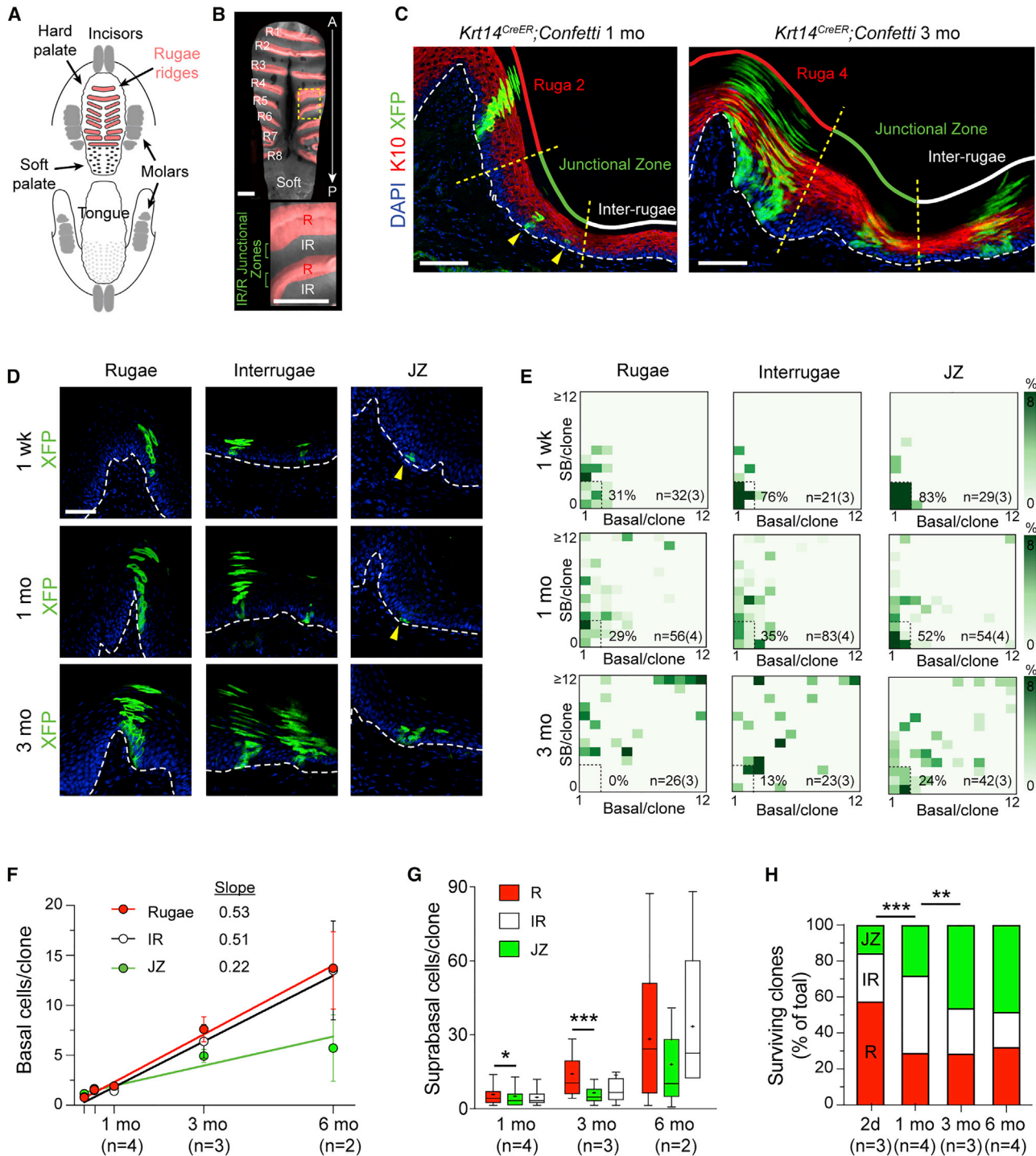


Figure 2. Lineage Tracing Reveals Regional Clonal Diversity within the HP

(A and B) Illustration (A) and whole mount (B) of the hard palate (HP) pseudocolored to demonstrate rugae (R1–R8, red) and inter-rugae regions (IR). The area within the dashed box is magnified below.

(C) 1 month and 3 month lineage tracing in *Krt14^{CreER};LSL-confetti* HP reveals different clone sizes among HP regions: rugae (R; red); junctional zone (JZ; green); and inter-rugae (IR; white). K10 (red) labels suprabasal (SB) differentiated cells.

(D and E) Representative images (D) and CDAs (E) of R, IR, and JZ after 1-week, 1-month, and 3-month chases. Arrows in (D) indicate small clones; boxed regions and percentages in (E) indicate latent clone frequency.

(F) Plot of basal cells/clone over time for each region; JZ grows most slowly up to 6 months.

(legend continued on next page)

and clone types in each tissue strongly suggests that division orientation dictates cell fate, at least within this labeling period.

Long-Term Lineage Tracing Reveals Unique Properties of HP Epithelium

Genetic lineage tracing represents a powerful means to determine how stem cell populations contribute to tissue growth and maintenance (Blanpain and Simons, 2013). To study regional growth dynamics in oral epithelia, we induced clones with a single dose of tamoxifen in *Krt14^{CreER}; LSL-Confetti* mice, and we harvested one month later. To display clone size distributions, we created clonal density arrays (CDAs, Figure 1G), where basal and SB cells per clone are plotted on x and y axes, respectively, and darker colors represent higher frequencies. We used CDAs to define four clone subtypes (Figure S1D): (1) latent (≤ 2 B and SB cells/clone), (2) basal-rich (B:SB ratio ≥ 3), (3) suprabasal-rich (SB:B ratio ≥ 3), and (4) balanced (all others).

Both VT and oropharynx favored balanced basal-layer expansion and SB differentiation, similar to what was recently reported in buccal OE (Jones et al., 2019) and consistent with stochastic fate choices/neutral drift (Klein and Simons, 2011). However, HP frequently displayed perpendicularly oriented columns of cells with one or few basal cells (Figure 1G, HP1); this was found in 50% of clones in the SB-rich subtype, compared to 10% and 6% in VT and oropharynx, respectively. In addition, latent clones (Figure 1G, HP2) were more numerous in HP (38%) compared to VT or oropharynx (10% and 8%, respectively), and 49% of HP clones consisted of a single basal cell, compared to 11% for VT and 23% for oropharynx (Figure 1H). Similar results were independently confirmed with the *Krt5^{CreER}* reporter (Figures S1E and S1F). Collectively, these data suggest that a high percentage of HP clones utilize a unique renewal pattern of invariant ACDs during homeostasis.

To follow clonal growth dynamics and turnover, we extended our lineage-tracing experiments out to 6 months. Consistent with neutral drift kinetics, all regions demonstrated a linear increase in basal cells/clone over time and a progressive decrease in surviving clone density (Figures 1I and 1J). Of note, however: HP displayed the slowest rate of increase in clone size over time and the highest proportion of surviving clones at late time points (Figure S1G). Thus, despite having similar proliferation rates, HP clones grow slower and have an increased probability of survival compared to VT and oropharynx clones. Together, these findings suggest that the HP harbors unusual proliferative heterogeneity.

Slow-Dividing OESCs Are Enriched in HP Junctional Zones, A Candidate Stem Cell Niche

The mammalian HP contains numerous rugae, which are mediolaterally-oriented, corrugated ridges thought to function together with the dorsal tongue in tactile sensation, bolus formation, and speech articulation (Moayedi et al., 2018; Peterková et al., 1987). Mice have between 8–9 rugae (R), subclassified

into antemolar (R1–R3) and intermolar (R4–R8) on the basis of their positions relative to the three maxillary teeth (Figures 2A and 2B). Ruga peaks are separated by valleys, termed inter-rugae (IR), of flattened epithelium.

Interestingly, most long-lived HP clones localized to the slopes of palatal rugae, at R/IR junctions (Figure S1G). Although the R and IR are delimited by molecularly distinct developmental programs (Welsh and O'Brien, 2009), no markers have been described to distinguish these regions in the adult. Therefore, we used morphological criteria (Figure 2C) to define the R region as the upper 50% of the ruga peaks; the IR region as the area between the inflection points of ruga slopes; and the junctional zone (JZ) as the lower 50% of the ruga slope, between the R and IR domains.

We employed CDAs to display clone distributions by location at 1 week, 1 month, and 3 months (Figures 2D and 2E). R clones appeared to expand most rapidly and tended to be SB-rich, with $\sim 1/3$ of clones consisting of >10 basal cells and >12 SB cells at 3 months. Although less expansive than R clones, IR clones were mostly of the SB-rich and balanced types. Conversely, JZ clones displayed an unusual bifurcation of clonal behavior by 3 months (basal-rich and SB-rich both represented $\sim 17\%$). While many clones consisted of 1–2 basal cells with multiple SB cells, consistent with invariant asymmetric expansion. A sizable minority of clones also expanded through SCDs with little differentiation (basal-rich + latent clone fraction = 41%). This behavior was uncommon in the R and IR (basal-rich + latent fraction = 0% for R and 26% for IR).

While basal cell numbers increased linearly with time in each region, the JZ also showed the lowest average number of basal cells/clone at all time points (Figure 2F). Moreover, the number of SB cells/clone was lowest in the JZ (Figure 2G), suggesting that they undergo comparatively less differentiation. Finally, in examining the location of surviving clones (Figure 2H), we noted that JZ clones persist, while R and IR clones are lost over time, demonstrating that JZ clones are long-lived. These data show that the JZ demonstrates unique growth behaviors and might be a stem cell niche for slow-dividing OESCs.

Label-Retaining Cells Reside in Discrete Niches in the HP Junctional Zone

Label-dilution assays represent another means to assess proliferation kinetics and identify populations of relative quiescence. Genetically, this can be accomplished by using doxycycline (dox)-regulable bipartite “tet-off” transgenics (*Krt5^{tTA}; tetO^{H2B-GFP}* or *K5-GFP*; Figure 3A). During the pulse period, stable histone H2B-GFP expression is initiated in all K5+ stratified epithelia, beginning during embryogenesis. Subsequent dox administration initiates the chase period, where existing label is diluted with each cell division (Tumbar et al., 2004). Because of subtle differences in K5/K14 expression seen across OE (Figure S2A), we also took a parallel approach with *Krt14^{Cre}; LSL^{tTA}; tetO^{H2B-GFP}* mice (*K14-GFP*), which we compared to the *K5-GFP* line (Figures 3B, 3C, S2B, and S2C).

(G) Tukey box-and-whisker plots (+, mean) comparing SB cells/clone and showing reduced differentiation in JZ compared to R.

(H) Quantification of surviving clone location over time reveals that JZ clones tend to be more persistent and long-lived compared to IR and R clones.

* $p < 0.05$, ** $p < 0.01$, and *** $p < 0.0001$, by Mann-Whitney test (G) and χ^2 (H). Scale bars: 500 μm (B); 100 μm (C), and 50 μm (D); n values in (F–H) indicate number of biological replicates.

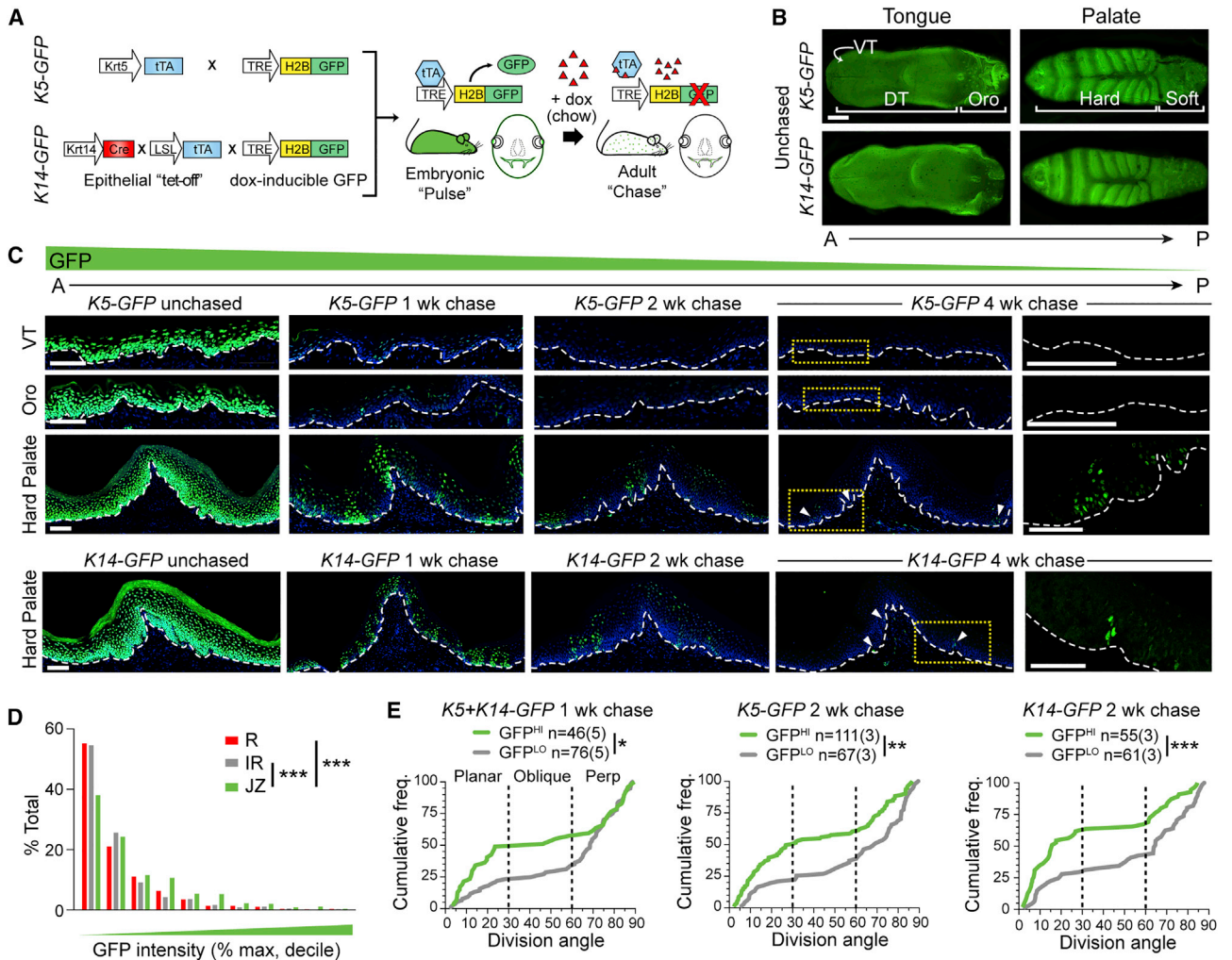


Figure 3. Label-Retaining Cells are Found in the Palate but Not in Other OEs

(A) Schematic of tet-off genetic label-retention assay. Induction was achieved in OE by using one of two promoters, *Krt5* or *Krt14*, with similar results. (B) Whole-mount images of H2B-GFP expression in unchased adult tongue and palate. VT = ventral tongue; DT = dorsal tongue; and Oro = oropharynx. (C) H2B-GFP+ label-retaining cells (LRCs) following 0-, 1-, 2-, and 4-week chase periods in indicated regions for *K5-GFP* (top three rows) and *K14-GFP* (bottom row) transgenics. Far right, high-magnification images of yellow, boxed regions at 4 weeks with DAPI (blue) removed; arrowheads indicate pockets of LRCs. (D) Quantification of GFP fluorescent intensity by region following a 2-week chase, binned into deciles. (E) Cumulative frequency plots of division orientation for GFP^{HI} (green) and GFP^{LO} (gray) HP cells from *K5-GFP* and *K14-GFP* mice, chased for 1 or 2 weeks. GFP^{HI} populations trend toward planar SCDs, whereas GFP^{LO} favor perpendicular ACDs. *n* values indicate cells and (biological replicates). Scale bars: 500 μ m (B) and 100 μ m (C). **p* < 0.05, ***p* < 0.01, and ****p* < 0.0001, by Kolmogorov-Smirnov test (D and E). See also Figure S2.

We first confirmed near-complete initial labeling (>95% of basal cells) of oral epithelia before chasing for 1, 2, or 4 weeks (Figures 3B and 3C). In lingual epithelia (tongue and oropharynx), GFP was rapidly diluted by 1 week and virtually absent by 2 weeks, whereas in the HP, discrete pockets of GFP+ label-retaining cells (LRCs) remained (Figures 3C, S2B, and S2C). Because post-mitotic sensory Merkel cells reside in palatal rugae (Moayed et al., 2018), we used β III-tubulin and p75/NGFR to label neuronal afferents, but we observed no colocalization with GFP (Figure S2D). Although rare, GFP+ LRCs were still detectable in the HP at 4 weeks with a GFP antibody, which enhanced the signal without altering label-retention kinetics (Figure S2E). In palatal whole mounts, LRCs were consistently

found in the JZ (Figure S2F), the same region where long-lived, basal-rich clones were observed (Figure S1G). Quantification of GFP intensity in *K5-GFP* mice chased for 2 weeks confirmed the highest levels of label retention in the JZ (Figure 3D).

Slow-Cycling Palatal LRCs Self-Renew through Planar Symmetric Divisions

Because label dilution was nearly complete after a 4-week chase, we deduced that LRCs were not truly quiescent, but, more accurately, were infrequently dividing cells (IDCs). We utilized three markers—Ki67 (cycling cells), pHH3 (mitotic cells), and 5-Ethynyl-2'-deoxyuridine/EdU (S-phase entry)—to compare proliferation between GFP^{HI} IDCs to GFP^{LO} frequently

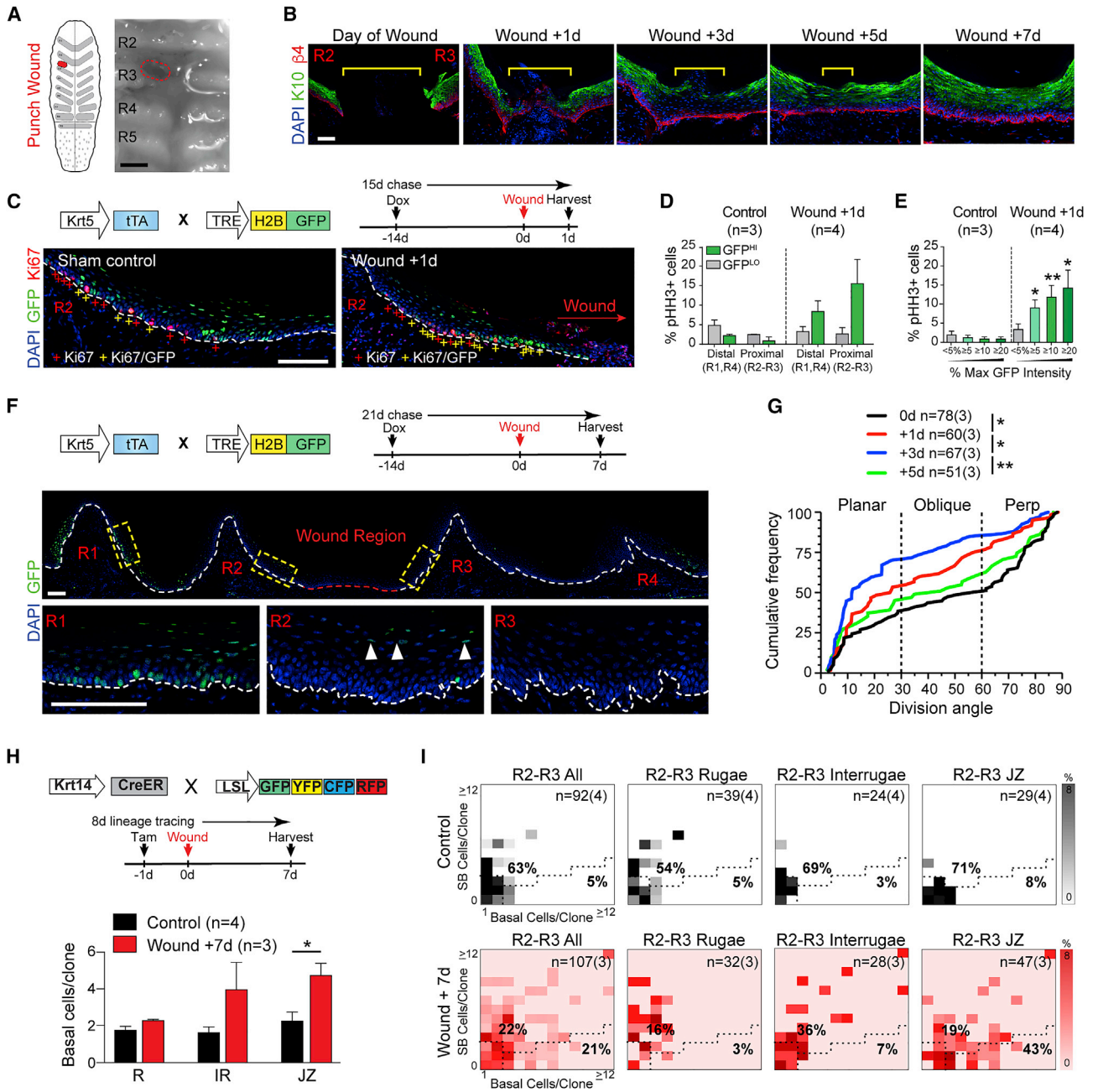


Figure 4. IDCs Are Recruited during Wound Repair

(A) Schematic (left) and stereoscope image (right) of a puncture wound in the IR space between R2 and R3. The dotted red line represents wound site.

(B) A wound healing timeline at 0, 1, 3, 5, and 7 days reveals rapid reapproximation (0–1 days) and reepithelialization (3–7 days). The yellow bracket shows the wound margin.

(C–E) *K5-GFP* mice chased for 2 weeks then wounded between R2–R3 and harvested 1 day later. (C) Colocalization of GFP+ LRCs with Ki67 in wound-proximal region in sham controls (left) and wound +1 day (right) palates; + signs: Ki67+ (red), GFP/Ki67 double-positive (yellow). Quantification of pHH3+ mitotic cells in IDC (GFP^H) and FDC (GFP^L) populations (D) and binned by GFP expression levels (E) for regions distal (R1 and R4) and proximal (R2 and R3) to the wound site. GFP^H populations become highly proliferative in the periwound area following injury.

(F) Image of wound region in *K5-GFP* mice chased for 2 weeks, wounded, and chased an additional 7 days. Loss of GFP label retention 7 days post-wound occurs specifically in wound-proximal rugae (R2/R3), but not in distal rugae (R1 and R4). Boxed regions are shown at higher magnification below; the remaining LRCs in R2 are largely SB cells (arrows).

(G) Cumulative frequency plot of division orientation in R2/R3 at 0, 1, 3, and 5 days post-wounding. Note transient switch toward planar SCDs 1–3 days post-wounding, recovering to a normal bimodal distribution by 5 days.

(legend continued on next page)

dividing cells (FDCs). As expected, cells with the highest GFP expression were the least proliferative (Figures S2G–K). Although GFP^{LO} FDCs were occasionally double-positive for EdU and pHH3, which is indicative of more rapid progression from S-phase into G2/M, no double-positive GFP^{HI} IDCs were observed (Figure S2L). We next asked whether IDCs and FDCs display distinct patterns of oriented cell divisions. In both *K5-GFP* and *K14-GFP* lines, GFP^{HI} IDCs displayed a high proportion of planar SCDs, whereas GFP^{LO} FDCs divided almost exclusively through perpendicular ACDs. These differences became more pronounced with longer chases (Figure 3E). Thus, IDCs are biased toward self-renewal, whereas FDCs exhibit a propensity for differentiation.

IDCs Are Mobilized by Symmetric Expansion during Wound Healing

OEs are remarkable in their capacity to heal more rapidly than skin and without scarring (Sciubba et al., 1978; Szpadarska et al., 2003). Recently, it was suggested that oral mucosa are “primed” for repair by expressing high levels of stem cell genes, such as Sox2, under homeostatic conditions; this process blocks differentiation during wound healing (Iglesias-Bartolome et al., 2018). To determine how the HP epithelium responds to injury, we developed an assay whereby a small puncture wound (~500 μm × 250 μm) is made in the largest (~1 mm) IR space between R2/R3 (Figure 4A). As expected, re-epithelialization was rapid: complete wound closure occurred by day 3, and normal epithelium was restored by day 7 (Figure 4B). Injury induced localized hyperproliferation adjacent to the wound site, which was evident as early as 1 day and abated by 7 days post-wounding (Figure S3A). Although proliferation was elevated throughout the anterior palate (R1–R4), the largest increase was localized to the wound proximal area (R2/R3), particularly in the first ~20 cells adjacent to the wound site (Figures S3B and S3C). This finding differs from what we see in the epidermis, where proliferation occurs behind a proximal migratory front (Aragona et al., 2017; Park et al., 2017).

The immediate, focal response to injury led us to hypothesize that wounding induces localized activation of IDCs. To test this, we chased *K5-GFP* mice for 2 weeks, puncture wounded, and assessed proliferation 1 day after wounding (Figure 4C). The GFP^{LO} population in both wound-distal (R1 and R4) and wound-proximal (R2 and R3) areas showed no change in pHH3+ cells after the injury. Conversely, IDCs responded to wounding by elevating mitotic activity, particularly in the wound-proximal area, and most dramatically in populations with the highest GFP levels (Figures 4D and 4E). We further predicted that if IDCs re-enter the cell cycle upon wounding, they should dilute their GFP^{HI} label after repair. To test this, we wounded 2-week-chased *K5-GFP* mice, then chased an additional 7 days during reepithelialization. This led to a near-complete local dilution of GFP at the wound site between R2 and R3, whereas IDCs could still be found in wound-distal R1 and R4 (Figure 4F).

Finally, because oral wound healing is thought to involve limiting differentiation (Iglesias-Bartolome et al., 2018), we asked whether injury affects division orientation. We observed a transient shift toward planar divisions that peaked 3 days post-wounding then returned to a homeostatic bimodal distribution by 5 days post-wounding (Figure 4G). Taken together, these data confirm that IDCs from the JZ respond to wounding by losing quiescence and expanding rapidly through SCDs to contribute disproportionately to reepithelialization of the wound bed.

Lineage Tracing Reveals that JZ OESCs Are Activated during Wound Healing

To determine how different HP regions respond to wounding, we adapted a strategy of genetic lineage tracing used previously in the epidermis (Mascré et al., 2012). We administered tamoxifen 1 day prior to wounding to establish clonal labeling and then harvested 7 days later once re-epithelialization was complete (Figure S3D). The JZ showed significant increase in the number of basal cells/clone, whereas the R was largely unaffected (Figures 4H and S3E). By using CDAs to display clonal composition, we show that both the JZ and IR showed a decrease in latent and increase in balanced clones (Figure 4I). Interestingly, we also observed a large increase in basal-rich clones following injury—from 8% to 43%—specifically in the JZ, suggesting that this region might be largely responsible for the expansion in planar SCDs observed after injury. Thus, basal cells in the JZ—and to a lesser extent, the IR—respond to injury by losing quiescence and rapidly proliferating/migrating into the wound region, whereas R clones contribute minimally to reepithelialization.

OESCs Are Sensitive to Physiologic Masticatory Stress

Our genetic lineage-tracing and label-retention studies revealed striking anterior-posterior differences across the HP epithelium. Specifically, we noted larger clones and more rapid label dilution in the posterior palate (Figures 5A and 5B). We hypothesized that this might be because of the position of the molars, which concentrate the mechanical forces experienced during mastication (Dutzan et al., 2017). To assess baseline levels of tissue turnover, we analyzed proliferation (Ki67-positivity) and *K5-GFP* intensity in each ruga following a 2-week chase. We observed inverse anterior-posterior gradients of proliferation and label retention, such that the highest proportion of Ki67+ cells was observed in intermolar rugae (R4–R8), while the greatest numbers of LRCs were observed in antemolar rugae (R1–R3) (Figures 5C, 5D, and S4A). On a per-cell basis, *K5-GFP* intensity was significantly higher in the anterior rugae, whether looking at the whole palate or the JZ alone (Figures 5C and S4A).

To test whether these anterior-posterior differences are caused by physiologic mastication stress, we compared tissue turnover rates in 2-week-chased *K5-GFP* mice fed standard pelleted hard dox chow versus softened chow (Figure 5E). We

(H and I) Lineage tracing using *K14^{CreER}; LSL-confetti* mice, which were treated with tamoxifen 1 day prior to wounding and harvested 7 days later. (H) Comparison of basal cells/clone by region in control and wounded animals. (I) CDAs outlining basal-rich clonal expansion in the JZ after wounding.

*p < 0.05 and **p < 0.01 by Kolmogorov-Smirnov (G) or Student's t test (D, E, and H); n values in (G and I) represent cells and (biological replicates) or biological replicates in (D, E, and H). Error bars are SEM. Scale bars: 100 μm. See also Figure S3.

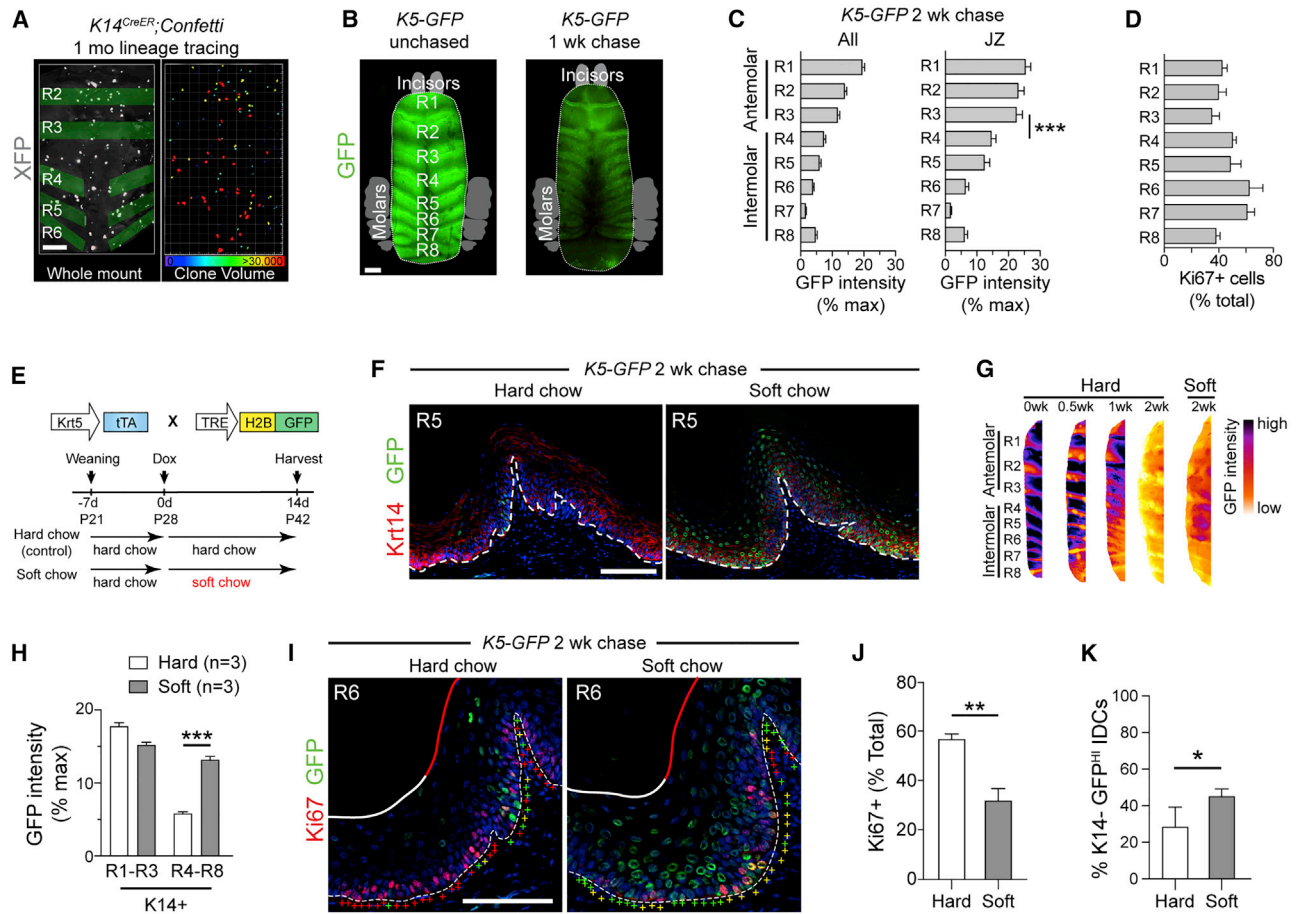


Figure 5. IDCs Are Sensitive to Physiologic Masticatory Forces

(A) 4-week lineage tracing of *K14^{CreER}; LSL-Confetti* whole-mount palate imaged with confocal microscope (RFP channel only) reveals a tendency toward larger clones by volume (μm^3) in the intermolar rugae (R5 and R6) compared to antimolar rugae (R2–R4). Clones were statistically color-coded for volume (right).

(B) Stereoscope image of 1-week-chased *K5-GFP* whole-mount palate revealing a tendency toward less GFP in the intermolar rugae compared to the antimolar rugae.

(C) Quantification of GFP label retention (% max intensity) by ruga shows significantly reduced levels in posterior HP compared to anterior whether comparing whole palate or JZ.

(D) Proliferation, as assessed by Ki67, across each ruga. Greater Ki67 positivity is observed in intermolar rugae.

(E) Schematic of label-retention assay in hard chow versus soft diet.

(F) Sagittal sections from *K5-GFP* mice chased for 2 weeks on hard or soft chow showing increased GFP in both basal (K14+) and suprabasal (K14-) cells on the soft diet.

(G) Intensity-coded images of LRC GFP expression in palate whole mounts for the chase periods indicated. Note both the AP gradient in label retention in the hard chow cohort, as well as the increased posterior label retention in the soft chow cohort.

(H) Quantification of GFP intensity binned by max GFP fluorescence in basal OESCs.

(I and J) Co-staining (I) for Ki67 and LRCs in hard (left) and soft (right) chow; + signs: Ki67+ (red), GFP+ (green), double positive (yellow). Overall frequency of cycling cells in posterior palate on soft chow is significantly reduced (J).

(K) Quantification of the percentage of *GFP^{HI}* IDCs that are SB (K14-) for hard and soft diet conditions. A greater proportion of IDCs are SB in the soft diet, which is indicative of decreased tissue turnover.

* $p < 0.05$, ** $p < 0.01$, and *** $p < 0.0001$, by Student's *t* test (C, H, J, and K). Error bars are SEM. Scale bars: 250 μm (A and B) and 100 μm (F and I). See also Figure S4.

hypothesized that a “low stress” soft diet might induce OESC quiescence, particularly in the posteriorly positioned, intermolar rugae. Soft chow indeed led to a dramatic increase in GFP+ cells, particularly in the posterior HP (Figures 5F, 5G, and S4B). This “anteriorization” of the posterior rugae was reflected by a >2-fold increase in mean GFP levels in the intermolar rugae after 2 weeks on a soft diet, accompanied by a significant decrease in Ki67+ cycling cells (Figures 5H–J).

To examine whether tissue turnover rates differ in hard and soft chow conditions, we compared the K14- (suprabasal) *GFP^{HI}* populations because these represent cells that have left the proliferative basal layer but have not yet terminally differentiated. As expected, soft diet increased mean GFP levels in both K14+ and K14- populations, particularly in posterior rugae (Figure S4D). Strikingly, the proportion of *GFP^{HI}* cells that are K14- increased from 28% in the hard diet

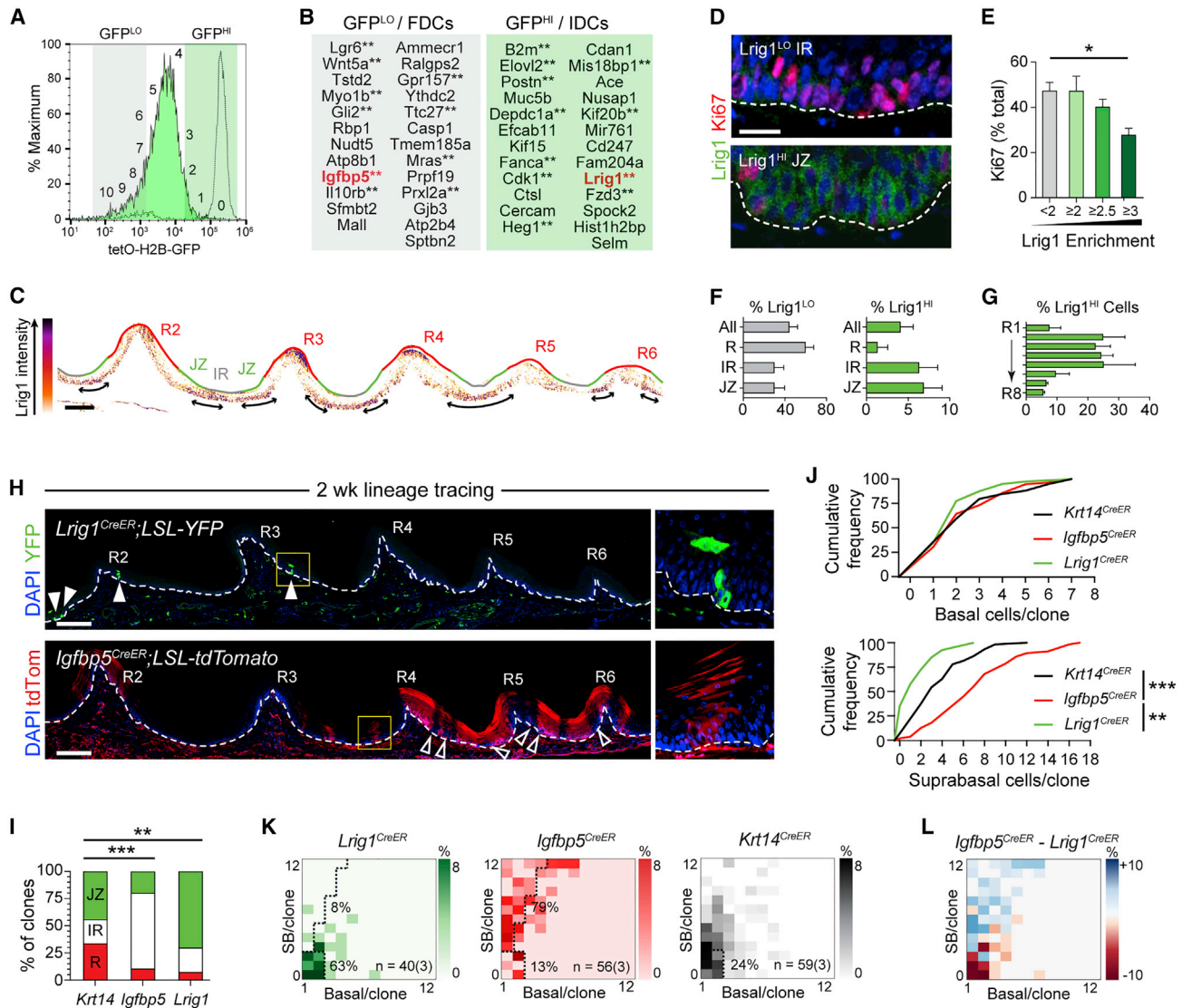


Figure 6. RNA-Seq and Lineage Tracing Reveal that Lrig1 Marks IDCs and Igfbp5 Marks FDCs

(A) FACS histogram of K5-GFP 2-week-chased GFP^{LO} (FDC) and GFP^{HI} (IDC) populations used for bulk RNA-seq analysis. The original GFP signal in the unchased K5-GFP is shown by a dashed line for reference.

(B) Top 25 significant differentially expressed genes in FDCs and IDCs with base mean greater than 25. Asterisks indicate genes that have reported roles in stem cell populations on the basis of a literature search. Genes in red indicate those used in this study for follow-up and validation.

(C) Lrig1 protein intensity plot of R2-R6. Double arrows indicate regions of highest Lrig1 enrichment.

(D and E) Co-labeling (D) of Lrig1 with Ki67. Lrig1^{LO} cells tend to be Ki67+, whereas Lrig1^{HI} cells are Ki67-; quantified in (E).

(F) Frequency of Lrig1^{LO} (defined as <math><2\times</math> over background) and Lrig1^{HI} (>3 \times over background) cells within each region.

(G) Lrig1^{HI} cell frequency by ruga, showing concentration in the anterior rugae.

(H) 2-week lineage tracing using *Lrig1*^{CreER} and *Igfbp5*^{CreER} drivers. White arrows in a *Lrig1*^{CreER} tile scan reveal small latent clones; the white open arrows in *Igfbp5*^{CreER} highlight unlabeled JZ. Zoomed-in images from the yellow dashed rectangles are at the right.

(I) Location of labeled clones for each driver line.

(J) Quantification of basal and SB cells/clone for each driver (*Krt14*^{CreER}, *Igfbp5*^{CreER}, and *Lrig1*^{CreER}) show most significant differences in SB cell count.

(K) CDAs of anterior clones for each driver. Note the high frequency of latent clones in *Lrig1*^{CreER} and the high frequency of SB-rich clones in *Igfbp5*^{CreER}.

(L) Subtractive CDA reveals enrichment of SB-rich clones in *Igfbp5*^{CreER} and latent clones in *Lrig1*^{CreER}.

* $p < 0.05$, ** $p < 0.01$, and *** $p < 0.0001$ by Student's t test (E), χ^2 (I), or Kolmogorov-Smirnov test (J). Error bars in are SEM. Scale bars: 100 μ m (C and H) and 20 μ m (D). $n = 3$ biological replicates per condition for (D-L). See also Figure S5.

condition to 45% in the soft diet condition (Figure 5K), consistent with the soft diet leading to slower tissue turnover. Collectively, these data demonstrate that OESCs are exquisitely

sensitive to physiological masticatory stresses that occur during normal feeding, and they respond to a soft diet by slowing proliferation and tissue turnover rates.

LRIG1 Is a Marker of IDCs

Next, we sought to identify genes that regulate OESC quiescence by performing transcriptional analysis of FACS-isolated GFP^{HI} IDCs and GFP^{LO} FDCs from 2-week-chased *K5-GFP* mice (Figures 6A and S5A). Among the list of differentially expressed genes (Figure 6B; Data S1), one of the most significantly enriched genes in the GFP^{HI} population was *Lrig1* (Leucine-rich repeats and immunoglobulin-like domains 1), which marks quiescent stem cell populations in numerous tissues (Choi et al., 2018; Jensen et al., 2009; Powell et al., 2012; Seidel et al., 2017). By using an LRIG1-specific antibody (for validation, see Figure S6A), we confirmed that LRIG1 was enriched in the JZ region where IDCs reside (Figure 6C). LRIG1^{HI} cells ($\geq 3\times$ expression over background) were less likely to be cycling compared to LRIG1^{LO} cells ($< 2\times$ over background), and quiescence became more pronounced with increasing LRIG1 expression (Figures 6D and 6E). LRIG1^{LO} cells were most frequently observed in the rugae, whereas LRIG1^{HI} cells were concentrated in the IR and JZ, and LRIG1^{HI} cells were more abundant in the anterior compared to posterior HP (Figures 6F, 6G, and S5B). Thus, overall LRIG1 is enriched in regions with less proliferation.

Lineage Tracing Reveals that IDCs Favor Self-Renewal and FDCs Favor Differentiation

To assess growth kinetics in IDC and FDC populations, we performed genetic lineage tracing with CreER reporter lines of genes enriched in IDCs (*Lrig1*), FDCs (*Igfbp5*), or expressed throughout the HP (*Krt14*). Of FDC signature genes, *Igfbp5* was of particular interest because of its enrichment in transit-amplifying populations in the interfollicular epidermis and tooth, as well as stem cells of the hair follicle bulge (Ichijo et al., 2017; Seidel et al., 2017; Tumber et al., 2004). Moreover, lineage tracing performed with *Lrig1*^{CreER} and *Igfbp5*^{CreER} in the incisor demonstrated that, despite both being expressed in the labial cervical loop stem cell compartment, *Igfbp5* clones grew rapidly and expanded distally into differentiated regions, whereas *Lrig1* clones remained smaller and closer to the quiescent region (Seidel et al., 2017).

We adjusted the tamoxifen regimen for each line in order to achieve sparse induction of clones and then performed lineage tracing for 2 weeks. *Lrig1*^{CreER}; *R26R*^{EYFP} clones were small, rare, and frequently observed in the anterior palate. On the other hand, *Igfbp5*^{CreER}; *R26R*^{tdTomato} clones were large, columnar, and enriched in the posterior palate, where they were too densely packed, even after a single low dose of tamoxifen, to distinguish individual clones (Figure 6H). Notably, even with near saturation labeling in the posterior HP, unlabeled gaps were frequently observed in the JZ (open arrows in Figure 6H). To induce sparser labeling in the *Igfbp5*^{CreER} line, we reduced the tamoxifen dose 6-fold and restricted our subsequent analyses of all three lines to clones found in R1–R3 (see Methods). We noted that the majority of *Lrig1* clones (70%) were found in the JZ, whereas conversely, 80% of *Igfbp5* clones were found in the IR or R (Figure 6I). Thus, the *Lrig1* and *Igfbp5* drivers label populations residing within distinct regions of the HP.

Although the average number of basal cells/clone was similar between all lines for this short 2-week labeling period, SB cell counts varied widely, with *Lrig1* clones containing significantly fewer and *Igfbp5* significantly more than *Krt14* clones (Figure 6J).

We next plotted basal and SB cell counts in CDAs for each driver (Figure 6K). *Lrig1* clones generally consisted of 1–2 basal cells and 4 or fewer SB cells (basal and latent clone fractions = 10% and 63%, respectively), whereas *Igfbp5* clones were large and contained many SB cells (SB-rich fraction = 79%; Figures 6K and S5C). To compare the clonal distributions of *Lrig1* and *Igfbp5* directly, we wrote a script to create a subtractive CDA (Figure 6L). This revealed that *Igfbp5* shows an enrichment of SB-rich clones, whereas *Lrig1* shows an enrichment in basal-rich clones (Figure 6L). These data suggest that *Lrig1* and *Igfbp5* label populations of OESCs that reside in distinct locations, with different growth kinetics, and that together, these two populations mirror the collective behavior of OESCs within the HP.

LRIG1^{HI} Cells Divide Symmetrically and Are IDCs

The small size and basal-rich nature of *Lrig1*^{CreER} clones suggested a predisposition to self-renewal. To ask whether LRIG1 expression levels correlate with preferences toward SCDs or ACDs, we analyzed division orientation in LRIG1^{HI} and LRIG1^{LO} populations. LRIG1^{LO} cells often divided through perpendicular ACDs, whereas LRIG1^{HI} cells displayed a high proportion of planar SCDs (Figure 7A). This divergent behavior mirrored what we observed with GFP^{HI} and GFP^{LO} populations in our label-retention studies (Figure 3E), with LRIG1^{HI} cells behaving like IDCs and LRIG1^{LO} cells like FDCs. LRIG1 immunostaining in 2-week-chased *K5-GFP* mice revealed a strong positive correlation between GFP and LRIG1 levels, particularly in the JZ (Figures 7B and 7C). Collectively, these findings indicate that LRIG1^{HI} cells and IDCs display similar characteristics of stemness and might represent the same population.

LRIG1 Expression Changes Dynamically in Response to Wounding and Mastication Stress

We next asked whether LRIG1 expression is altered under conditions where IDCs are either activated (wounding) or maintained in a more quiescent state (soft diet). Because wounding induces rapid local proliferation within the IDC population near the wound site, we examined LRIG1 expression in 2-week-chased *K5-GFP* mice 1 day post-wounding. As expected, wounding induced local OESC proliferation, as measured by Ki67 expression within the IDC population (Figure 7D). This was accompanied by downregulation of LRIG1 expression in the wound area and an increase in the proportion of LRIG1+ cells that entered the cell cycle (Figures 7E and 7F). Conversely, a 2-week soft diet in *K5-GFP* chased mice led to a significant decrease in proliferation and an increase in the number of GFP^{HI} IDCs in posterior rugae, which correlated with an increase in LRIG1 expression (Figures 7G–7I). Thus, LRIG1 expression is diminished by stress-inducing wounding and elevated by a stress-mitigating soft diet.

LRIG1 Loss Leads to a Loss of Quiescence during Homeostasis

We next assessed how *Lrig1* loss affects quiescence by using a null *Lrig1-Apple* knockin reporter allele (Poulin et al., 2014). We first confirmed that the LRIG1 antibody is coexpressed with the endogenous reporter in control *Lrig1*^{Ap/+} heterozygotes and that LRIG1 antibody staining was lost in the JZ of *Lrig1*^{Ap/Ap}

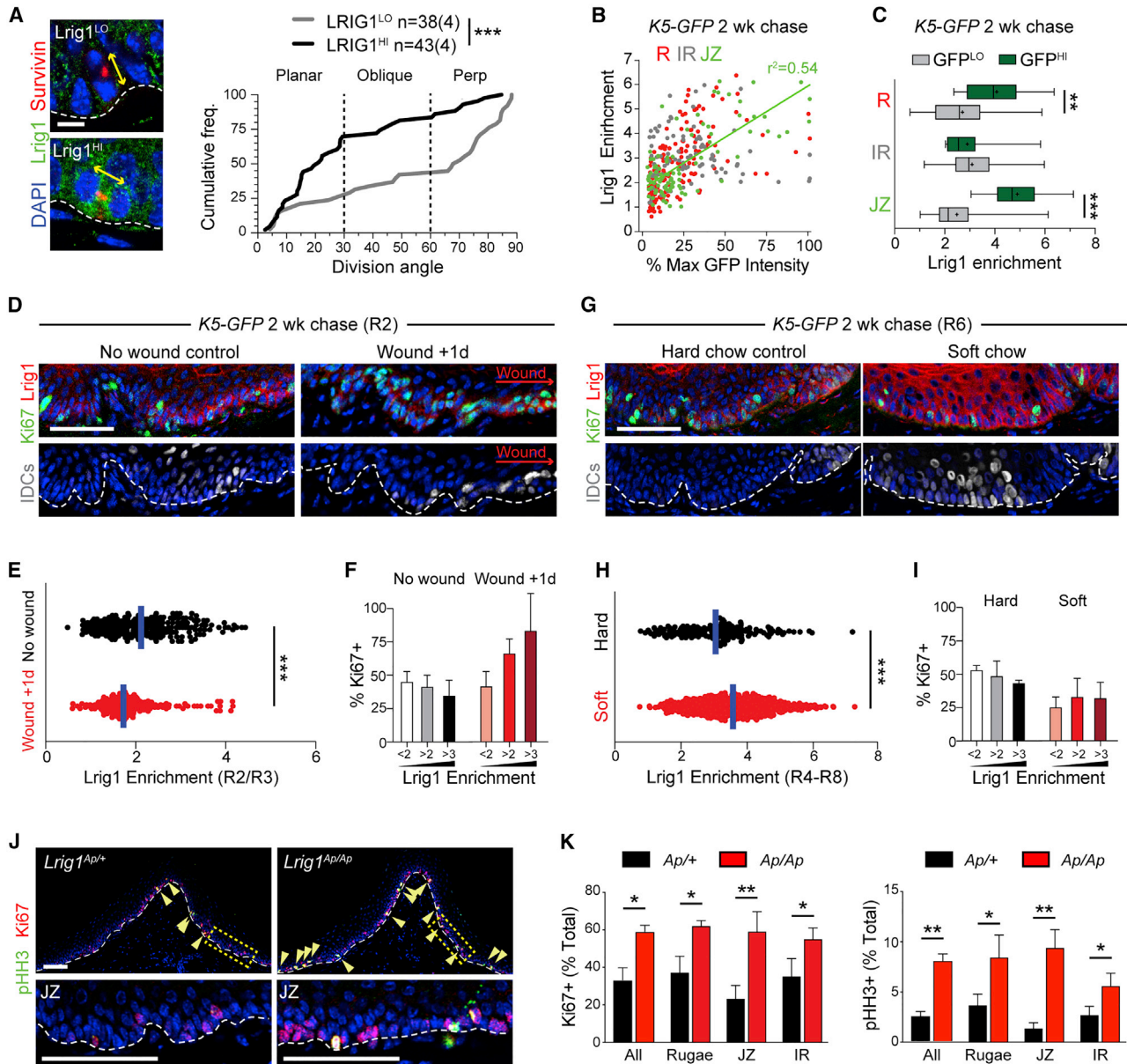


Figure 7. Lrig1 Adapts OESCs to Tissue Stress and Maintains Quiescence

(A) Cumulative frequency distribution of division orientation for $Lrig1^{LO}$ (gray) and $Lrig1^{HI}$ (black) populations. Like IDCs (Figure 3E), $Lrig1^{HI}$ cells frequently execute planar divisions.

(B) GFP intensity (% max) plotted against Lrig1 enrichment for cells located within the JZ (green), R (red), or IR (white). There is a strong positive correlation for the JZ (green line; $r^2 = 0.54$).

(D–F) R2 region in $K5-GFP$ mice chased for 2 weeks, 1 day after wounding.

(D) Lrig1 decreases in early wound healing as cycling concomitantly increases. Note that many IDCs near the wound site are Ki67+.

(E) Quantification of Lrig1 expression levels in periwound area 1 day after wounding (red) and in unwounded controls (black).

(F) Frequency of Ki67+ cells in $Lrig1^{LO}$ (<2x enrichment), $Lrig1^{MED}$ (2–3-fold enrichment), and $Lrig1^{HI}$ (>3-fold enrichment) populations. $Lrig1^{HI}$ cells, normally quiescent, re-enter the cell cycle 1 day after wounding.

(G–I) R6 region in $K5-GFP$ mice chased for 2 weeks on either hard or soft diet.

(G) Lrig1 levels increase in the soft diet as cycling (Ki67+) decreases.

(H) Quantification of Lrig1 expression levels in intermolar rugae, showing a significant increase in Lrig1 expression on the soft diet.

(I) Ki67+ cell frequency binned by Lrig1 levels for hard and soft diet conditions. The soft diet leads to a global decrease in cycling.

(legend continued on next page)

nulls (Figure S6A). Although no obvious differences were observed in division orientation in the HP between *Lrig1^{Ap/AP}* nulls and *Lrig1^{Ap/+}* controls (Figure S6B), a clear difference was observed in proliferation. Both pHH3 and Ki67 were significantly upregulated in *Lrig1^{Ap/AP}* nulls compared to in controls (Figures 7J, 7K, S6C, and S6D). Most of the increased proliferation could be attributed to loss of quiescence in the JZ, where the proportion of pHH3+ mitotic cells increased from $1.36 \pm 0.34\%$ to $9.4 \pm 1.06\%$, a 7-fold change (Figure 7K). Comparatively, the R and IR regions showed a modest ~2-fold increase in pHH3 positivity. Collectively, these data indicate that LRIG1 is an important regulator of OESC quiescence under homeostatic conditions.

DISCUSSION

Our studies show that there are important inter- and intra-regional differences by which OESCs self-renew in the oral cavity. Among the tissues studied here, the HP is unique in displaying marked proliferative heterogeneity and for containing a regional niche where slow-cycling OESCs reside. IDCs reside in the JZ and primarily self-renew through SCDs, whereas FDCs of the IR and R are biased toward differentiative ACDs. Similar behaviors are observed with LRIG1^{Hi} and LRIG1^{Lo} populations, respectively, and *Lrig1* loss leads to a striking loss of quiescence, particularly in the JZ. IDCs are sensitive to both stress-inducing (wounding) and stress-mitigating (soft diet) events, which evoke opposite proliferative responses. Wounding induces a localized response whereby JZ IDCs are disproportionately activated to self-renew through SCDs and migrate into the wound bed to promote reepithelialization. Collectively, these data demonstrate that JZ IDCs possess many defining characteristics of “reserve” stem cells: quiescence, self-renewal by SCD, LRIG1 expression, and activation after injury.

Our analysis of oriented cell divisions and short-term lineage tracing (Figures 1B–F) reveal many important similarities—as well as differences—among OEs. The fraction of clones that had undergone at least one division at 48 h was 48% for HP, 58% for oropharynx, and 56% for VT (Figure 1F). These data are consistent with the estimated average cell-cycle length of ~2 days in the buccal epithelium (Jones et al., 2019), while also revealing that the HP is overall more quiescent despite the rapid renewal in the rugae. Additionally, delamination appears to be an important contributor to differentiation—representing ~1/3 of all clones in each tissue—and was more common than ACDs (Figure 1F). Notably, the delamination:SCD ratio in the VT and oropharynx was nearly balanced (0.82 and 0.86, respectively), consistent with a model of delamination driving local tissue differentiation, as proposed in the adult epidermis (Mesa et al., 2018). However, the delamination:ACD ratio varied widely between tissues (3.03 in VT versus 1.64 in HP), suggesting that ACDs might supplement delamination to

drive differentiation in high-turnover regions, such as the rugae ridges, that experience greater stress.

We also noted a strong correlation between division orientation and ACD:SCD clone ratios across all tissues, suggesting that oriented cell divisions dictate fate choices in oral epithelia. Notably, however, in some tissues, particularly oropharynx, the fraction of delamination clones decreased while the ACD fraction increased from 24 h to 48 h (Figure 1F). It is likely that some of these ACD clones might actually represent an “asymmetric” planar division where one daughter subsequently delaminates after mitosis, as has been observed in the epidermis (Rompolas et al., 2016). This notion is supported by scRNA-seq data, which revealed that buccal OESCs frequently initiate differentiation in the basal layer (Jones et al., 2019). Both this study and our data (Figure S3A) report that K14 expression is heterogeneous in the basal layer, suggesting that K14^{Lo} basal cells might be in the process of differentiating.

The favored model of stem cell dynamics in stratified epithelia—based on mathematical modeling of clonal evolution in genetic lineage-tracing studies—has been termed population asymmetry/neutral drift (Clayton et al., 2007; Jones et al., 2007). This model of stochastic competition has been shown to predict stem cell behaviors in a wide variety of tissues, including the intestine, epidermis, and seminiferous tubules (Klein and Simons, 2011). The mucosal buccal epithelium also adheres to this model (Jones et al., 2019), and in agreement with these findings, we find that VT and oropharynx rapidly and uniformly dilute *K5/K14-GFP* label (Figures 3C, S2B, and S2C). However, although the HP also displays scaling behavior of linear expansion of stem cell number/clone as a function of time (Figure 1I), we noted significant differences in growth rates and differentiation behaviors between the JZ and other palatal regions (Figures 2D–2H). Of note, the IR and JZ were the only regions to contain completely undifferentiated clones (exclusively basal cells), even at the 12-week time point (8.7% and 14.3%, respectively). Whether there is a hierarchical relationship between IDCs and FDCs or whether they exist as separate, regional stem cell pools remains to be determined. We favor the latter hypothesis because we rarely observed clonal expansion across HP zones even in our longest lineage-tracing experiments.

It is interesting to note that in the epidermis, genetic lineage tracing revealed that “transit-amplifying” (*Inv^{CreER}*) and “stem cell” (*Krt14^{CreER}*) populations show different potential in wound-healing assays, with *Krt14* cells contributing substantially—and *Inv* cells minimally—to reepithelialization (Mascre et al., 2012). This is, in many ways, similar to what we observe with the differential wound-healing capacity of the JZ relative to other palatal populations, such as the R and IR (Figures 6H and 6I). Ultimately, lineage tracing with the *Lrig1^{CreER}* and *Igfbp5^{CreER}* lines after wounding could further clarify the relative contributions of distinct HP populations to reepithelialization.

LRIG1 marks stem cells in the GI tract (Choi et al., 2018; Powell et al., 2012) and the hair follicle (Jensen et al., 2009; Jensen and

(J and K) Expression of proliferation markers in control (*Lrig1^{Ap/+}*) and *Lrig1* null (*Lrig1^{Ap/AP}*) HP. Arrowheads indicate mitotic (pHH3+; green) cells. The boxed areas of JZ are shown at higher magnification below.

(K) Quantification of Ki67 (left) and pHH3 (right) positivity, demonstrating significantly increased proliferation in *Lrig1^{Ap/AP}* nulls, particularly in JZ region.

p* < 0.05, *p* < 0.01, and ****p* < 0.0001 by Student's *t* test, except for Kolmogorov-Smirnov in (A). Error bars in are SEM. Scale bars: 100 μm (J), 50 μm (D and G), and 10 μm (A). *n* = 3 biological replicates for D–K. See also Figure S6.

Watt, 2006). Although it seems to perform a similar function in palatal epithelium, our RNA-seq data (Data S1) suggest that *Lrig1* is expressed at relatively low levels compared to other stem cell compartments. In support of this, we performed lineage tracing with two different *Lrig1*^{CreER} lines (Page et al., 2013; Powell et al., 2012) and using single and multiple low tamoxifen doses in a week, and although we observed sparse labeling throughout the oral cavity at 2 weeks, we could only detect rare clones in the HP epithelium, in agreement with a recent study (Jones et al., 2019). Ultimately, we required both higher and multiple doses (5× over one week, 15 mg tamoxifen total) to achieve sufficient labeling. Nonetheless, we provide several strong lines of evidence that LRIG1 maintains OESC quiescence in the palatal epithelium: (1) LRIG1 colocalizes with IDCs, (2) clones are smaller and have higher LRIG1 expression in the antemolar rugae where proliferation rates are lower; (3) LRIG1^{Hi} and LRIG1^{Lo} populations display distinct patterns of oriented cell division that match IDCs and FDCs, respectively; (4) LRIG1 is upregulated in the more quiescent posterior palate on a soft diet; (5) LRIG1 expression decreases after wounding as IDCs lose quiescence; and (6) *Lrig1* loss induces a massive increase in proliferation, particularly in the JZ.

This work illustrates how both environmental and genetic influences affect regional OESC activity. The striking change to OESC activity in the posterior rugae as a result of a simple change in diet was a surprising result, and this finding demonstrates how homeostasis in the oral cavity is a dynamic process that can incorporate daily functional stressors. It is tempting to consider how the microenvironment of neuronal afferents and Merkel cells—which are known to be highly concentrated in posterior rugae JZ and rarer in antemolar rugae (Moayedi et al., 2018)—might be able to signal to OESCs for increased/decreased activity. Whether it is because the JZ is protected from masticatory stresses, a signaling niche, or both, IDCs consistently localize to this region. Developmentally, these HP junctional zones are well delineated by various markers, including *Shh* (rugae-specific) and *Sostdc1* (interrugae-specific) (Welsh and O'Brien, 2009), suggesting the possible existence of unique, region-specific transcriptional programs that are important for OESC behaviors. It is also interesting that HP is an uncommon site for oral cancers in humans (Bagan et al., 2010; Cerami et al., 2012). Knowledge of the transcriptional and cellular programs that regulate HP OESC behavior might yield important insights into why this tissue is refractory to transformation.

STAR★METHODS

Detailed methods are provided in the online version of this paper and include the following:

- KEY RESOURCE TABLE
- LEAD CONTACT AND MATERIALS AVAILABILITY
- EXPERIMENTAL MODEL DETAILS
 - Mouse Husbandry and Experimental Conditions
 - Mouse Lines
- METHOD DETAILS
 - Fluorescence Immunohistochemistry
 - Genetic Lineage Tracing
 - Genetic Label-Retention Assays

- Flow Cytometry
- RNA-Sequencing
- Softened Chow Experiments
- Wound Healing
- Imaging Acquisition
- QUANTIFICATION AND STATISTICAL ANALYSES
 - Differential Gene Expression Analysis
 - Clonal Density Arrays
 - GFP Label-Retention Intensity Quantification
 - Quantification of Oriented Cell Division Vectors
 - Quantification of Ki67⁺, EdU⁺, and pHH3⁺ Cells
 - Clone Size Quantification from Whole Mounts
 - Quantification of LRIG1 Enrichment
 - Statistical Analyses
- DATA AND CODE AVAILABILITY

SUPPLEMENTAL INFORMATION

Supplemental Information can be found online at <https://doi.org/10.1016/j.stem.2019.11.005>.

ACKNOWLEDGMENTS

We thank the Tabin and Goodrich (Harvard) and Amelio labs (University of North Carolina [UNC]) for sharing mice. We are grateful to members of the Williams, Klein, Coffey, and Watt labs for helpful discussions. We thank Matteo Battilocchi for coordinating mouse experiments, as well as Susan Henning, Scott Magness, and Carlton Anderson (UNC Advanced Analytics Core) for technical advice. Funding: K08 DE026537 (K.M.B.), Center for Gastrointestinal Biology & Disease (supported by P30 KD034987) (S.E.W.), Kimmel Scholar Award SKF-15-165 (S.E.W.), P50 CA095103 (R.J.C.), R35 CA197570 (R.J.C.), and R35 DE026602 (O.D.K.).

AUTHOR CONTRIBUTIONS

Conceptualization and Methodology, K.M.B. and S.E.W.; Investigation, K.M.B., N.C.P., J.H.P., W.J.H., I.S., and P.M.; Resources, W.J.H., I.S., P.M., F.M.W., O.D.K., and R.J.C.; Software, N.J.P.; Writing – Original Draft, S.E.W. and K.M.B.; Writing – Review & Editing, S.E.W., K.M.B., K.J.L., and O.D.K.; Supervision, S.E.W., F.M.W., R.J.C., and O.D.K.; Funding Acquisition, S.E.W. and K.M.B.

DECLARATION OF INTERESTS

The authors declare no competing interests.

Received: December 20, 2018

Revised: September 12, 2019

Accepted: November 13, 2019

Published: December 5, 2019

REFERENCES

- Alcolea, M.P., Greulich, P., Wabik, A., Frede, J., Simons, B.D., and Jones, P.H. (2014). Differentiation imbalance in single oesophageal progenitor cells causes clonal immortalization and field change. *Nat. Cell Biol.* 16, 615–622.
- Aragona, M., Dekoninck, S., Rulands, S., Lenglez, S., Mascré, G., Simons, B.D., and Blanpain, C. (2017). Defining stem cell dynamics and migration during wound healing in mouse skin epidermis. *Nat. Commun.* 8, 14684.
- Arwert, E.N., Hoste, E., and Watt, F.M. (2012). Epithelial stem cells, wound healing and cancer. *Nat. Rev. Cancer* 12, 170–180.
- Asaka, T., Akiyama, M., Kitagawa, Y., and Shimizu, H. (2009). Higher density of label-retaining cells in gingival epithelium. *J. Dermatol. Sci.* 55, 132–134.
- Bagan, J., Sarrion, G., and Jimenez, Y. (2010). Oral cancer: Clinical features. *Oral Oncol.* 46, 414–417.

- Bickenbach, J.R. (1981). Identification and behavior of label-retaining cells in oral mucosa and skin. *J. Dent. Res.* *60 Spec No C*, 1611–1620.
- Bickenbach, J.R., and Mackenzie, I.C. (1984). Identification and localization of label-retaining cells in hamster epithelia. *J. Invest. Dermatol.* *82*, 618–622.
- Blanpain, C., and Fuchs, E. (2009). Epidermal homeostasis: A balancing act of stem cells in the skin. *Nat. Rev. Mol. Cell Biol.* *10*, 207–217.
- Blanpain, C., and Simons, B.D. (2013). Unravelling stem cell dynamics by lineage tracing. *Nat. Rev. Mol. Cell Biol.* *14*, 489–502.
- Byrd, K.M., Lough, K.J., Patel, J.H., Descovich, C.P., Curtis, T.A., and Williams, S.E. (2016). LGN plays distinct roles in oral epithelial stratification, filiform papilla morphogenesis and hair follicle development. *Development* *143*, 2803–2817.
- Cerami, E., Gao, J., Dogrusoz, U., Gross, B.E., Sumer, S.O., Aksoy, B.A., Jacobsen, A., Byrne, C.J., Heuer, M.L., Larsson, E., et al. (2012). The cBio cancer genomics portal: An open platform for exploring multidimensional cancer genomics data. *Cancer Discov.* *2*, 401–404.
- Choi, E., Lantz, T.L., Vlachich, G., Keeley, T.M., Samuelson, L.C., Coffey, R.J., Goldenring, J.R., and Powell, A.E. (2018). Lrig1+ gastric isthmal progenitor cells restore normal gastric lineage cells during damage recovery in adult mouse stomach. *Gut* *67*, 1595–1605.
- Clayton, E., Doupé, D.P., Klein, A.M., Winton, D.J., Simons, B.D., and Jones, P.H. (2007). A single type of progenitor cell maintains normal epidermis. *Nature* *446*, 185–189.
- Doupé, D.P., Alcolea, M.P., Roshan, A., Zhang, G., Klein, A.M., Simons, B.D., and Jones, P.H. (2012). A single progenitor population switches behavior to maintain and repair esophageal epithelium. *Science* *337*, 1091–1093.
- Dutzan, N., Abusleme, L., Bridgeman, H., Greenwell-Wild, T., Zangerle-Murray, T., Fife, M.E., Bouladoux, N., Linley, H., Brenchley, L., Wemyss, K., et al. (2017). On-going mechanical damage from mastication drives homeostatic Th17 cell responses at the oral barrier. *Immunity* *46*, 133–147.
- Gur, G., Rubin, C., Katz, M., Amit, I., Citri, A., Nilsson, J., Amariglio, N., Henriksson, R., Rechavi, G., Hedman, H., et al. (2004). LRIG1 restricts growth factor signaling by enhancing receptor ubiquitylation and degradation. *EMBO J.* *23*, 3270–3281.
- Hsu, Y.C., Li, L., and Fuchs, E. (2014). Emerging interactions between skin stem cells and their niches. *Nat. Med.* *20*, 847–856.
- Ichijo, R., Kobayashi, H., Yoneda, S., Iizuka, Y., Kubo, H., Matsumura, S., Kitano, S., Miyachi, H., Honda, T., and Toyoshima, F. (2017). Tbx3-dependent amplifying stem cell progeny drives interfollicular epidermal expansion during pregnancy and regeneration. *Nat. Commun.* *8*, 508.
- Iglesias-Bartolome, R., Uchiyama, A., Molinolo, A.A., Abusleme, L., Brooks, S.R., Callejas-Valera, J.L., Edwards, D., Doci, C., Asselin-Labat, M.-L., and Onaitis, M.W. (2018). Transcriptional signature primes human oral mucosa for rapid wound healing. *Science Transl. Med.* *10*, eaap8798.
- Ipponjima, S., Hibi, T., and Nemoto, T. (2016). Three-dimensional analysis of cell division orientation in epidermal basal layer using intravital two-photon microscopy. *PLoS ONE* *11*, e0163199.
- Jensen, K.B., and Watt, F.M. (2006). Single-cell expression profiling of human epidermal stem and transit-amplifying cells: Lrig1 is a regulator of stem cell quiescence. *Proc. Natl. Acad. Sci. USA* *103*, 11958–11963.
- Jensen, K.B., Collins, C.A., Nascimento, E., Tan, D.W., Frye, M., Itami, S., and Watt, F.M. (2009). Lrig1 expression defines a distinct multipotent stem cell population in mammalian epidermis. *Cell Stem Cell* *4*, 427–439.
- Jones, K.B., and Klein, O.D. (2013). Oral epithelial stem cells in tissue maintenance and disease: The first steps in a long journey. *Int. J. Oral Sci.* *5*, 121–129.
- Jones, P.H., Simons, B.D., and Watt, F.M. (2007). Sic transit gloria: Farewell to the epidermal transit amplifying cell? *Cell Stem Cell* *7*, 371–381.
- Jones, K.B., Furukawa, S., Marangoni, P., Ma, H., Pinkard, H., D'Urso, R., Zilionis, R., Klein, A.M., and Klein, O.D. (2019). Quantitative Clonal Analysis and Single-Cell Transcriptomics Reveal Division Kinetics, Hierarchy, and Fate of Oral Epithelial Progenitor Cells. *Cell Stem Cell* *24*, 183–192.e8.
- Klein, A.M., and Simons, B.D. (2011). Universal patterns of stem cell fate in cycling adult tissues. *Development* *138*, 3103–3111.
- Laederich, M.B., Funes-Duran, M., Yen, L., Ingalla, E., Wu, X., Carraway, K.L., 3rd, and Sweeney, C. (2004). The leucine-rich repeat protein LRIG1 is a negative regulator of ErbB family receptor tyrosine kinases. *J. Biol. Chem.* *279*, 47050–47056.
- Lechler, T., and Fuchs, E. (2005). Asymmetric cell divisions promote stratification and differentiation of mammalian skin. *Nature* *437*, 275–280.
- Love, M.I., Huber, W., and Anders, S. (2014). Moderated estimation of fold change and dispersion for RNA-seq data with DESeq2. *Genome Biol.* *15*, 550.
- Lu, M.S., and Johnston, C.A. (2013). Molecular pathways regulating mitotic spindle orientation in animal cells. *Development* *140*, 1843–1856.
- Mascre, G., Dekoninck, S., Drogat, B., Youssef, K.K., Broheé, S., Sotiropoulou, P.A., Simons, B.D., and Blanpain, C. (2012). Distinct contribution of stem and progenitor cells to epidermal maintenance. *Nature* *489*, 257–262.
- Mesa, K.R., Kawaguchi, K., Cockburn, K., Gonzalez, D., Boucher, J., Xin, T., Klein, A.M., and Greco, V. (2018). Homeostatic epidermal stem cell self-renewal is driven by local differentiation. *Cell Stem Cell* *23*, 677–686.e4.
- Moayed, Y., Duenas-Bianchi, L.F., and Lumpkin, E.A. (2018). Somatosensory innervation of the oral mucosa of adult and aging mice. *Sci. Rep.* *8*, 9975.
- Morin, X., and Bellaïche, Y. (2011). Mitotic spindle orientation in asymmetric and symmetric cell divisions during animal development. *Dev. Cell* *21*, 102–119.
- Nowak, J.A., and Fuchs, E. (2009). Isolation and culture of epithelial stem cells. *Methods Mol. Biol.* *482*, 215–232.
- Page, M.E., Lombard, P., Ng, F., Göttgens, B., and Jensen, K.B. (2013). The epidermis comprises autonomous compartments maintained by distinct stem cell populations. *Cell Stem Cell* *13*, 471–482.
- Papagerakis, S., Pannone, G., Zheng, L., About, I., Taqi, N., Nguyen, N.P., Matossian, M., McAlpin, B., Santoro, A., McHugh, J., et al. (2014). Oral epithelial stem cells - implications in normal development and cancer metastasis. *Exp. Cell Res.* *325*, 111–129.
- Park, S., Gonzalez, D.G., Guirao, B., Boucher, J.D., Cockburn, K., Marsh, E.D., Mesa, K.R., Brown, S., Rompolas, P., Haberman, A.M., et al. (2017). Tissue-scale coordination of cellular behaviour promotes epidermal wound repair in live mice. *Nat. Cell Biol.* *19*, 155–163.
- Peterková, R., Klepáček, I., and Peterka, M. (1987). Prenatal development of rugae palatinae in mice: Scanning electron microscopic and histologic studies. *J. Craniofac. Genet. Dev. Biol.* *7*, 169–189.
- Potten, C.S. (1974). The epidermal proliferative unit: The possible role of the central basal cell. *Cell Tissue Kinet.* *7*, 77–88.
- Poulin, E.J., Powell, A.E., Wang, Y., Li, Y., Franklin, J.L., and Coffey, R.J. (2014). Using a new Lrig1 reporter mouse to assess differences between two Lrig1 antibodies in the intestine. *Stem Cell Res. (Amst.)* *13* (3 Pt A), 422–430.
- Powell, A.E., Wang, Y., Li, Y., Poulin, E.J., Means, A.L., Washington, M.K., Higginbotham, J.N., Juchheim, A., Prasad, N., Levy, S.E., et al. (2012). The pan-ErbB negative regulator Lrig1 is an intestinal stem cell marker that functions as a tumor suppressor. *Cell* *149*, 146–158.
- Rompolas, P., Mesa, K.R., Kawaguchi, K., Park, S., Gonzalez, D., Brown, S., Boucher, J., Klein, A.M., and Greco, V. (2016). Spatiotemporal coordination of stem cell commitment during epidermal homeostasis. *Science* *352*, 1471–1474.
- Sada, A., Jacob, F., Leung, E., Wang, S., White, B.S., Shalloway, D., and Tumber, T. (2016). Defining the cellular lineage hierarchy in the interfollicular epidermis of adult skin. *Nat. Cell Biol.* *18*, 619–631.
- Sciubba, J.J., Waterhouse, J.P., and Meyer, J. (1978). A fine structural comparison of the healing of incisional wounds of mucosa and skin. *J. Oral Pathol.* *7*, 214–227.
- Seidel, K., Marangoni, P., Tang, C., Houshmand, B., Du, W., Maas, R.L., Murray, S., Oldham, M.C., and Klein, O.D. (2017). Resolving stem and progenitor cells in the adult mouse incisor through gene co-expression analysis. *eLife* *6*, e24712.
- Seldin, L., and Macara, I. (2017). Epithelial spindle orientation diversities and uncertainties: Recent developments and lingering questions. *F1000Res.* *6*, 984.

- Suzuki, Y., Miura, H., Tanemura, A., Kobayashi, K., Kondoh, G., Sano, S., Ozawa, K., Inui, S., Nakata, A., Takagi, T., et al. (2002). Targeted disruption of *LIG-1* gene results in psoriasiform epidermal hyperplasia. *FEBS Lett.* *521*, 67–71.
- Szpaderska, A.M., Zuckerman, J.D., and DiPietro, L.A. (2003). Differential injury responses in oral mucosal and cutaneous wounds. *J. Dent. Res.* *82*, 621–626.
- Tumbar, T., Guasch, G., Greco, V., Blanpain, C., Lowry, W.E., Rendl, M., and Fuchs, E. (2004). Defining the epithelial stem cell niche in skin. *Science* *303*, 359–363.
- Wang, Y., Shi, C., Lu, Y., Poulin, E.J., Franklin, J.L., and Coffey, R.J. (2015). Loss of *Lrig1* leads to expansion of Brunner glands followed by duodenal adenomas with gastric metaplasia. *Am. J. Pathol.* *185*, 1123–1134.
- Welsh, I.C., and O'Brien, T.P. (2009). Signaling integration in the rugae growth zone directs sequential SHH signaling center formation during the rostral outgrowth of the palate. *Dev. Biol.* *336*, 53–67.
- Willberg, J., Syrjänen, S., and Hormia, M. (2006). Junctional epithelium in rats is characterized by slow cell proliferation. *J. Periodontol.* *77*, 840–846.
- Williams, S.E., Beronja, S., Pasolli, H.A., and Fuchs, E. (2011). Asymmetric cell divisions promote Notch-dependent epidermal differentiation. *Nature* *470*, 353–358.
- Williams, S.E., Ratliff, L.A., Postiglione, M.P., Knoblich, J.A., and Fuchs, E. (2014). *Par3-mInsc* and *Gzi3* cooperate to promote oriented epidermal cell divisions through LGN. *Nat. Cell Biol.* *16*, 758–769.

STAR★METHODS

KEY RESOURCE TABLE

REAGENT or RESOURCE	SOURCE	IDENTIFIER
Antibodies		
Rabbit anti-survivin (71G4B7) (1:1000 dilution)	Cell Signaling	Cat# 2808; RRID:AB_2063948
Chicken anti-GFP (1:2000 dilution)	Abcam	Cat# ab13970; RRID:AB_300798
Rat anti-mCherry (16D7) (1:2000 dilution)	Thermo Fisher Scientific	Cat# M11217; RRID:AB_2536611
Guinea Pig anti-cytokeratin 5 (1:1000 dilution)	Acris Antibodies GmbH	Cat# BP5006; RRID:AB_979709
Chicken anti-cytokeratin 14 (Poly9060) (1:1000 dilution)	BioLegend	Cat# 906001; RRID:AB_2565055
Rabbit anti-p75 NGF Receptor (EP1039Y) (1:500 dilution)	Abcam	Cat# ab52987; RRID:AB_881682
Mouse anti-class III beta-Tubulin (1:1000 dilution)	BioLegend	Cat# 801202; RRID:AB_10063408
Rat anti-Ki67 (SolA15) (1:500 dilution)	Thermo Fisher Scientific	Cat# 14-5698-80; RRID:AB_10853185
Rabbit anti-histone H3, phospho (Ser10) (1:1000 dilution)	Millipore	Cat# 06-570; RRID:AB_310177
Goat anti-Lrig1 (1:100 dilution)	R&D Systems	Cat# AF3688; RRID:AB_2138836
Rabbit anti-cytokeratin 10 (Poly19054) (1:1000 dilution)	BioLegend	Cat# 905404; RRID:AB_2616955
Donkey anti-rabbit IgG Alexa Fluor 488 (1:1000 dilution)	Molecular Probes	Cat# A-21206; RRID:AB_141708
Donkey anti-rat IgG Alexa Fluor 488 (1:1000 dilution)	Molecular Probes	Cat# A-21208; RRID:AB_141709
Donkey anti-guinea pig IgG Alexa Fluor 488 (1:1000 dilution)	Jackson ImmunoResearch Labs	Cat# 706-545-148; RRID:AB_2340472
Donkey anti-goat IgG Alexa Fluor 488 (1:1000 dilution)	Jackson ImmunoResearch Labs	Cat# 705-546-147; RRID:AB_2340430
Donkey anti-chicken IgG Alexa Fluor 488 (1:1000 dilution)	Jackson ImmunoResearch Labs	Cat# 703-545-155; RRID:AB_2340375
Donkey anti-rabbit IgG Rhodamine Red-X (1:500 dilution)	Jackson ImmunoResearch Labs	Cat# 711-295-152; RRID:AB_2340613
Donkey anti-rat IgG Rhodamine Red-X (1:500 dilution)	Jackson ImmunoResearch Labs	Cat# 705-175-147; RRID:AB_2340415
Donkey anti-guinea pig IgG Rhodamine Red-X (1:500 dilution)	Jackson ImmunoResearch Labs	Cat# 706-295-148; RRID:AB_2340468
Donkey anti-goat IgG Rhodamine Red-X (1:500 dilution)	Jackson ImmunoResearch Labs	Cat# 705-295-003; RRID:AB_2340422
Donkey anti-chicken IgG Rhodamine Red-X (1:400 dilution)	Jackson ImmunoResearch Labs	Cat# 703-296-155; RRID:AB_2340372
Donkey anti-rabbit IgG Cy5 (1:400 dilution)	Jackson ImmunoResearch Labs	Cat# 711-175-152; RRID:AB_2340607
Donkey anti-rat IgG Cy5 (1:400 dilution)	Jackson ImmunoResearch Labs	Cat# 712-295-150; RRID:AB_2340675
Donkey anti-guinea pig IgG Cy5 (1:400 dilution)	Jackson ImmunoResearch Labs	Cat# 706-175-148; RRID:AB_2340462
Donkey anti-goat IgG Cy5 (1:400 dilution)	Jackson ImmunoResearch Labs	Cat# 705-175-147; RRID:AB_2340415
Donkey anti-chicken IgG Cy5 (1:400 dilution)	Jackson ImmunoResearch Labs	Cat# 703-175-155; RRID:AB_2340365
Rabbit anti-RFP Pre-adsorbed (1:100 dilution)	Rockland	Cat# 600-401-379; RRID:AB_2209751
Rat anti-CD49f-Alexa Fluor® 647 (PS/2) (1:50 dilution)	BioLegend	Cat# 313609; RRID:AB_493636

(Continued on next page)

Continued

REAGENT or RESOURCE	SOURCE	IDENTIFIER
Critical Commercial Assays		
Click-iT Plus EdU Alexa Fluor 647 kit	Thermo Fisher Scientific	Cat# C10640
Sytox® Dead Cell Stain	Thermo Fisher Scientific	Cat# S34857
Other		
Tamoxifen	Sigma-Aldrich	Cat# T5648
Dispase	Life Technologies	Cat# 17105-041
Teklad Custom Diet: Rodent Diet (625 Dox, R)	Envigo (https://www.envigo.com/)	Cat# TD.08541
Powder Control Liquid Diet	Envigo (https://www.envigo.com/)	Cat# TD.170605.PWD
Germinator 500 Glass Bead Decontaminator	Roboz	Cat# DS-401
16G x 1 1/2" PrecisionGlide Needles, Regular Bevel, Sterile	BD	Cat# 305198
Liquid Diet Feeding Tube	Bio-Serv	Cat# 9019
Liquid Diet Feeding Tube Holder, Short	Bio-Serv	Cat# 9015
Davidson Marking System® Blue from 7-Color Set of 3cc (3ml) Dyes	Bradley Products (https://www.bradleyproducts.com/)	Cat# 1007-P
Deposited Data		
GitHub	https://github.com/byrdkm/oral-stem	CDAs: cda-original Subtractive CDAs: cda-diff
GEO	https://www.ncbi.nlm.nih.gov/geo/	GSE139146
Experimental Models: Mouse Lines		
Tg(KRT14-cre/ERT)20Efu	Jackson Laboratory	Cat# 005107
Krt5 ^{tm1.1(cre/ERT2)Blh}	Jackson Laboratory	Cat# 029155
Gt(ROSA)26Sortm1(CAG-Brainbow2.1)Cle	Jackson Laboratory	Cat# 013731
FVB/N-Tg(KRT5-tTA)1216G1k/Nci	NCI Mouse Repository	Cat# 01XM8
Tg(KRT14-cre)1Amc/J	Jackson Laboratory	Cat# 004782
B6.129P2(Cg) Gt(ROSA)26Sortm1(tTA)Roos/J	Jackson Laboratory	Cat# 011008
Tg(tetO-HIST1H2BJ/GFP)47Efu	Jackson Laboratory	Cat# 005104
Lrig1 ^{mAppleC1}	(Poulin et al., 2014)	N/A
Lrig1 ^{CreERT2/+} ; RosaR26R ^{EYFP/EYFP (cis)}	(Wang et al., 2015)	N/A
Igfbp5 ^{CreERT2/+} ; RosaR26R ^{tdTomato}	(Seidel et al., 2017)	N/A
Software and Algorithms		
FIJI		https://imagej.net/Fiji
Bitplane Imaris, v8.4		http://www.bitplane.com/
GraphPad Prism, v7		https://www.graphpad.com/scientific-software/prism/
Origin 2016		https://www.originlab.com/2016
FlowJo, v10		https://www.flowjo.com/
Python 3.6.4		https://www.python.org/
Plotly		https://plot.ly/
Adobe Photoshop CS6		https://www.adobe.com/products/photoshop
Adobe Illustrator CS6		https://www.adobe.com/products/illustrator
DESeq2	(Love et al., 2014)	https://bioconductor.org/packages/release/bioc/html/DESeq2.html

LEAD CONTACT AND MATERIALS AVAILABILITY

Requests for further information should be directed to and will be fulfilled by the Lead Contact, Scott Williams (scott_williams@med.unc.edu). This study did not generate new unique reagents.

EXPERIMENTAL MODEL DETAILS

Mouse Husbandry and Experimental Conditions

All mice were maintained, manipulated, and harvested in an AAALAC certified animal facility under IACUC approved protocols and were monitored daily by certified veterinarian technicians daily at the University of North Carolina at Chapel Hill. For research, we use carbon dioxide and physical euthanasia in accordance with the Panel on Euthanasia of the American Veterinary Medical Association to euthanize animals. For all experiments: at least two animals were used for each analysis, including both males and females. Each of the animals were determined to be ‘healthy’/body score 3; animals that deviated from health or housing conditions were not included in these studies. For each experiment, no animals had previously been included in any other experiments. Animals were housed according to IACUC guidelines on ‘standard housing’ with ‘environmental enrichment’ (including group housing compatible animals and providing animals nest building materials) in the same racks at UNC—or at UCSF for the *Igfbp5^{CreER}* lineage-tracing experiments. The trained veterinarian technicians worked daily to accomplish the following tasks: to facilitate animal well-being for research, providing adequate cage space and a comfortable environment with 12 h light/dark cycles that is escape-proof but with appropriate ventilation, making food (Envigo Rodent Irradiated 2920x) and water easy to access *ad libitum*, washing and changing cages to clean and maintain the environment free from hazards, alerting the lab to changes in health conditions, and providing the availability to monitor the mice at least once per 24 h period.

Mouse Lines

The following mouse lines were obtained from collaborators: 1) Tg(KRT14-cre)1Amc/J (*Krt14^{Cre}*; The Jackson Laboratory, Jax strain 004782); Dougald Monroe (UNC); 2) Tg(KRT14-cre/ERT)20Efu (*Krt14^{CreER}*; Jax strain 005107); Tony Amelio (UNC). The following strain was obtained from the National Cancer Institute Mouse Repository: FVB/N-Tg(KRT5-tTA) (*Krt5^{tTA}*; strain 01XM8). The following strains were obtained from The Jackson Laboratory: 1) *Krt5tm1.1(cre/ERT2)Blh* (*Krt5^{CreER}*; Jax strain 029155); 2) Gt(ROSA)26Sortm1(CAG-Brainbow2.1)Cle (*LSL-Confetti*; Jax strain 013731); 3) B6.129P2(Cg) *Gt(ROSA)26Sortm1(tTA)Roos/J* (*LSL^{tTA}*; Jax strain 011008); and 4) Cd1/Tg(tetO-HIST1H2BJ/GFP) (*TRE^{H2B-GFP}*; Jax strain 005104). *Lrig1^{mAppleC1}* (referred to as *Lrig1^{Ap/+}* or *Lrig1^{Ap/Ap}*; (Poulin et al., 2014)) and *Lrig1^{CreERT2/+}*; *RosaR26R^{EYFP/EYFP}* (Powell et al., 2012; Wang et al., 2015) strains were maintained, manipulated, and harvested in an AAALAC certified animal facility under IACUC approved protocols at Vanderbilt University. *Igfbp5^{CreER}*; *RosaR26^{tdTomato}* (Seidel et al., 2017) mice were maintained, manipulated, and harvested in an AAALAC certified animal facility under IACUC approved protocols at the University of California, San Francisco. *Krt5^{CreER}* and *Krt14^{CreER}* mice were crossed with *LSL-Confetti* mice to generate heterozygous or homozygous reporter mice for lineage-tracing experiments. *K14^{Cre}* mice were crossed with *LSL^{tTA}* mice to generate heterozygous or homozygous driver mice. *Krt5^{tTA}* and *K14^{Cre}*; *LSL^{tTA}* mice were mated with *TRE^{H2B-GFP}* to generate heterozygous *K5-GFP* or *K14-GFP* mice for label-retaining experiments. At least two animals were used for each analysis and all mice were between 4-12 weeks old, except for the *Lrig1^{Ap}* experiments in Figures 7 and 6S, which were 12 months old.

METHOD DETAILS

Fluorescence Immunohistochemistry

Tissues were microdissected into cold 1x PBS and fixed for 30 min at room temperature (RT) in 4% paraformaldehyde (PFA). After washing with PBS 3x/10min at RT, samples were equilibrated sequentially in 15% and 30% sucrose solutions at 4°C, and then mounted in Tissue-Tek optimal cutting temperature (OCT) compound (Electron Microscopy Services). 12 μm sagittal sections were cut on a Leica CM1950 cryostat onto SuperFrost Plus slides (Thermo Fisher Scientific) and stored at -80°C. Samples were dried at 37°C for 30 min before a 1 h incubation with gelatin block (5% normal donkey serum, 1% BSA, 2% gelatin, and 0.1% Triton X-100 in 1x PBS). Slides were incubated with primary antibodies diluted in gelatin block O/N at 4°C and washed 3x/5min in 1x PBS at RT. Secondary antibodies were also diluted in gelatin block and added to the slide for 2 h at RT. DAPI (1:2000 dilution) was added to the slide for 5 min at RT; samples were mounted in 100 μL ProLong Gold (Invitrogen) and covered by glass coverslips (Thermo Fisher). All mice from label-retaining cell assays were injected intraperitoneally (IP) with a dose of 50 μg/g body weight EdU (Life Technologies) 2 h before harvest. EdU Click-iT® (Thermo Fisher) chemical reactions were performed on slides for 30 min according to manufacturer’s protocol before performing the described secondary antibody protocol.

Genetic Lineage Tracing

Male and Female adult (between 4-12 weeks old) *Krt5^{CreER}*; *LSL-Confetti* and *Krt14^{CreER}*; *LSL-Confetti* mice were given a single IP dose (30 mg/kg and 100 mg/kg body weight, respectively) of tamoxifen (Sigma-Aldrich) and harvested 24 h, 36 h, 48 h, 1 week, 2 weeks, 1 month, 3 months, and 6 months later. Male and female adult (between 4-12 weeks old) *Lrig1^{CreERT2/+}*; *RosaR26R^{EYFP/EYFP(cis)}* and *Igfbp5^{CreER}*; *RosaR26^{tdTomato}* mice were given doses of IP tamoxifen (5x injections over 1 week at

120 mg/kg, and 1x injection at 20 mg/kg, respectively) and harvested 2 weeks after the last tamoxifen dose. Sagittal sections (≥ 2 animals/time point, ≥ 2 slides, and ≥ 5 sections/slide) were stained for K10, RFP and GFP. The *LSL-Confetti* mice, the anti-GFP antibody (Abcam) labels and enhances three of the four *Confetti* reporters, each with distinct subcellular localization patterns (nuclear GFP, membranous CFP, and cytoplasmic YFP) that allow clones to be easily distinguished. 20x/1.5x optical zoom single field images were acquired for every labeled clone. For long-term lineage-tracing experiments (Figures 2D–2H), tile-scan composite images were taken of the entire palate region (Figure S11). For comparisons between the *Lrig1^{CreER}*, *Krt14^{CreER}*, and *Igfbp5^{CreER}* lines (Figures 6H–6L), only clones in anterior rugae (R1–R3) were analyzed because the labeling density was too high to resolve single clones in R4–R8 of the *Igfbp5^{CreER}* line. Clones deemed as being too close to one another, which was defined as any clone where the anterior or posterior extension of the clone (suprabasal or basal fraction) was less than 10 cells away from the nearest clone, were excluded from these analyses.

For 24, 36, and 48 h experiments (Figure 1), each clone each clone was categorized as follows: 1) asymmetric cell division (ACD; one basal cell and one suprabasal cell); 2) symmetric cell division (SCD; two basal cells); 3) single basal cells (non-mitotic); 4) delaminating (non-mitotic, single suprabasal cell in spinous layer); or 5) ≥ 2 cell clones (multiple divisions within the labeling period). Clones were categorized as 1) single basal cells if no labeled SB cell was seen surrounding the clone in the z stack and 2) delaminating if no labeled basal cell was seen surrounding the clone in the z stack and the clone was in the first third of the differentiated cell layers (spinous layer only).

Genetic Label-Retention Assays

Genetic label-retention studies are based on the previous work of (Tumbar et al., 2004), which utilized *Krt5^{tTA}* and *tetO^{H2B-GFP}* mice. We used this combination of strains (*K5-GFP*) as well as the triple transgenic *Krt14^{Cre};LSL^{tTA};tetO^{H2B-GFP}* (*K14-GFP*) line. GFP levels were readily detectable at birth using a fluorescent flashlight (NIGHTSEA DFP-1). To initiate the “chase” period, by inhibiting new expression of H2B-GFP, male and female adult *K5-GFP* and *K14-GFP* mice between 4–12 weeks of age were switched to pelleted doxycycline chow (Harlan TD.08541 Rodent Diet: 2018, Teklad Global 18% Protein Rodent Diet 999.175 g/kg, 0.625 g/kg Doxycycline Hyclate, Red Food Color 0.2g/kg) for 0, 3, 7, 14, or 28 days. Doxycycline chow was kept refrigerated at 4°C and away from light until use.

Flow Cytometry

Hard palates (rugae 1–8) were microdissected and immediately transferred to 12-well plates with 1 mL of PBS and kept on ice. 500 μ L 1x dispase (Life Technologies) was added to each palate and incubated for 1 h at 37°C. Dissecting forceps (Roboz) were used to peel the epithelia from the underlying lamina propria and scissors/forceps were used to physically separate the epithelia into smaller pieces. Further isolation of basal palatal cells was adapted from the epidermal method of (Nowak and Fuchs, 2009). Palatal epithelia were transferred to a new 12-well plate with 0.25% Trypsin-EDTA. After 60 min incubation at 37°C with vigorous shaking, samples were triturated with P1000 pipette tips precoated with FACS buffer (PBS + 1% FBS) several times to suspend basal epithelial cells. Single cells were isolated using a 35 μ m Falcon cell strainer (Thermo Fisher), rinsed with 2 mL of epidermal low calcium medium (E low Ca²⁺, and then centrifuged for 5 min at RT/300x g. The cell pellet was resuspended in FACS buffer and stored on ice. To isolate basal cells by FACS, Rat anti-CD49f-Alexa Fluor® 647 ($\alpha 6$ -Integrin, BioLegend) was added to cells and incubated for 60 min on ice. Sytox® Dead Cell Stain (Thermo Fisher, 1:1000) was added 5 min before FACS to evaluate cell viability. FACS was performed on a Sony SH800S Cell Sorter, with the following single-channel compensation controls: unchased GFP palatal epithelial cells, anti-CD49f:Alexa Fluor® 647 negative, and Sytox® Dead Cell Stain negative cell suspensions. Flow cytometry analyses were performed using FlowJo 10 software.

RNA-Sequencing

RNA was isolated from 200–1000 cells and libraries prepared using the SoLo RNA-Seq library preparation kit (NuGEN). Paired-end RNA sequencing was performed at the UNC High Throughput Sequencing Facility on an Illumina HiSeq4000 with 150 cycles. ~ 30 million reads were obtained per sample. Illumina output data were first processed using Illumina’s bcl2fastq pipeline (v.2.20.0). Quality control of the samples was performed using FastQC.

Softened Chow Experiments

For soft chow experiments (Figures 5E–5K and 7G–7I), hard chow was mechanically pulverized into a fine powder using a mallet. Twenty grams of doxycycline chow (Harlan) was added to a 10-cm Petri dish (Falcon), and weighed with an automatic scale to determine the amount of water required. Paste was made by slowly adding mouse drinking water to pulverized chow until the mass ratio of water:food was 1.5 (30 g water per 20 g dox chow for 50 g paste/Petri dish). New soft dox chow was freshly made every day. Male and female adult *K5-GFP* were chased for 2 weeks as described using the pelleted “hard” chow or using the pulverized “soft” chow until harvest.

Wound Healing

Male and female adult mice (4–12 weeks old) were anesthetized in an induction chamber with 1L/min O₂ and 3% isoflurane vapor. Animals were switched from the induction chamber to the nose cone attached to a homemade aluminum-coated surgical platform. An assistant opened the mouth mediolaterally and superoinferiorly for visual access using two pairs of blunted surgical forceps

(Roboz). Puncture wounds were made using a 16 gauge (g) needle (Becton Dickinson) that was heated using a Bunsen burner and bent at a 90° only at the beveled tip. Autoclaved wounding tips were coated in blue dye (Davidson marking system; Bradley Products) to label the wound site immediately before making a small puncture wound in the right interrugae space (between R2-R3) with the wider wound measurement oriented mediolaterally (Figure 4A). Mice were placed on a liquid diet (Envigo; TD.170605.PWD) for 5 days following wounding and weighed daily. Briefly, this powdered diet is based on the Lieber-DeCarli liquid diet formulation. To make the liquid diet, molecular grade water (mL) was measured powdered diet (g) to approximate a liquid/diet ratio of 4.5mL/g. The diet was mixed for about 30 s by vigorously shaking in glassware with a lid. Liquid chow was prepared fresh daily. The dry powder was kept refrigerated at 4C for \leq 6 months and was stored away from light post-manufacturing. Liquid chow was given to a cage of up to 3 animals using Liquid Diet Feeding Tube (Bio-Serv). Meloxicam was injected 1x/day (5mg/mL) at 24 and 48 h post-wounding to alleviate post-surgical pain. Pilot studies included animals that were harvested on 0, 1, 3, 5, and 7 days post-wounding to assess for wound healing timelines.

For genetic lineage-tracing experiments (Figures 4H and 4I), male and female adult *Krt14^{CreER};LSL-Confetti* mice were given a single dose intraperitoneally of tamoxifen (100 mg/kg body weight). Animals were wounded one day after tamoxifen injection and then harvested 7 post-wounding (8 days total). Sagittal sections (\geq 3 animals/time point) from wounded and matched unwounded animals were stained for K10, RFP and GFP. Only the anterior rugae (R1-R4) around the wound site were imaged and analyzed.

For genetic label-retention experiments, male and female adult *K5-GFP* animals were chased for 2 weeks using doxycycline chow. Animals were wounded according to the standard protocol with only a minor accommodations for soft chow. In the 1-day wounding studies (Figures 4C–4E), wounded and unwounded control animals were given pulverized ‘soft’ chow in Petri dishes for 24 h before harvest. In the 7-day studies (Figure 4F), wounded and unwounded control animals were given pulverized ‘soft’ chow in Petri dishes for 2 days before switching back to ‘hard’ dox chow for 5 days before harvest 7 days after wounding.

Imaging Acquisition

All images are displayed in an anteroposterior orientation from left to right and with the spinous layers superior to the basal layer, irrespective of 3D anatomical orientation. For sections, images were acquired using LAS X software on a Leica TCS SPE-II 4 laser confocal system on a DM5500 upright microscope with ACS Apochromat 10x/0.30 air, ACS Apochromat 20x/0.60 multi-immersion, ACS Apochromat 40x/1.15 oil, and ACS Apochromat 63x/1.30 oil objectives. Lineage tracing and oriented cell division images were acquired at 20x/1.5 and 63x/3.0x optical zoom, respectively, using between 9–12 z stacks spaced every 2–3 μ m to examine the whole section. For whole field label-retention and proliferation experiments, images were acquired at 20x/1.5x optical zoom using the tile scan feature from the center of the section as determined by DAPI and stitched together using the LAS X mosaic merge “statistical” feature. For confocal wholemount imaging (Figure 3E), which included a combination of tile scans and z stacks, z-volume was determined using endogenous GFP signal from the *K14-GFP* and the endogenous RFP signal from the *Krt14^{CreER};LSL-Confetti* reporter, optical section thickness was manually manipulated for thicker slices (10 μ m) to preserve fluorescent signal. For stereoscope wholemount imaging (Figures 2B, 4A, and 5B), images were acquired with a Leica M165 FC using Leica V4.7 software. All image analysis was performed using FIJI. All Images were edited using Adobe Photoshop CS6/CC and figures were created using Adobe Illustrator CS6/CC.

QUANTIFICATION AND STATISTICAL ANALYSES

Differential Gene Expression Analysis

RNA-seq fastq files were trimmed and aligned to the latest mouse genome, mm10 (GRCm38/GCA_000001635.2) using BBMap. A matrix of the data was generated using featureCounts. RNA-seq data were analyzed with DESeq2 (Love et al., 2014), excluding one sample that was an extreme outlier by PCA analysis and two samples that had very poor quality scores. All statistical analyses were performed using R version 3.4.1 and RStudio version 1.0.143.

Clonal Density Arrays

In order to display three-dimensional data from lineage-tracing data (suprabasal cells/clone, basal cells/clone, and frequency), we developed clonal density arrays (CDAs), which were inspired by (Alcolea et al., 2014). Scripts to create CDA plots were generated with python 3.6.4, input into Plotly (<https://plot.ly>), and are available at [GitHub.com](https://github.com/byrdkm/oral-stem/cda-original) (byrdkm/oral-stem/cda-original). Each array uses the same cut-off (8% of total clonal distribution) for consistency. CDAs also allow us to easily visualize several distinct types of clone: 1) “latent” (B: < 2 cells and SB: < 2 cells/clones), 2) “basal-rich” (B:SB Ratio >3), 3) “suprabasal-rich” (SB:B ratio >3), and 4) “balanced” (all others). See Figure S1F for an example, including annotations. In Figure 6L, the subtractive CDA was also generated with python 3.6.4, input into Plotly: see [GitHub.com](https://github.com/byrdkm/oral-stem/cda-diff) (byrdkm/oral-stem/cda-diff). The average Lrig1 CDA values were subtracted from the Igfbp5 CDA values to demonstrate clonal density differences between the two populations. On a color value spectrum from blue to red, the difference between CDA basal, SB cell coordinates (x, y) were assigned a color between >10% labeled “blue” to \geq 10% (“red”).

GFP Label-Retention Intensity Quantification

K5-GFP and *K14-GFP* tissues were processed for immunofluorescence, including enhancing the GFP signal with chicken anti-GFP antibody (1:2000; Abcam). Unchased (Day 0) *K5-GFP* and *K14-GFP* tissues were used to adjust the confocal parameters to the

maximum saturated EGFP fluorescence intensity at baseline. These settings were used for the various chase intervals. Tile-scan confocal images of the entire palate region were acquired at 20x/1.5x optical zoom. GFP fluorescence values were calculated by manually measuring fluorescence intensity (a.u.) using the FIJI Multi-point tool (type: dot, color: yellow, size: large) in every basal DAPI+ cell from anterior to posterior in 1) every experimental condition, 2) in multiple slides ($n \geq 2$), and 3) in multiple embryos ($n \geq 3$). Blinding to GFP intensity was accomplished by using the DAPI channel to select nuclei for analysis. Raw values were captured and binned between $< 5\%$, $\geq 5\%$, $\geq 10\%$, $\geq 20\%$, and $\geq 50\%$ of max.

Quantification of Oriented Cell Division Vectors

Measurement of division orientation is relative to the basement membrane (indicated by dashed lines) and relies on using the late stage mitotic marker survivin to delineate the position of the two daughter cells, as has been described previously (Williams et al., 2011). Briefly, the vector that bisects the two daughter nuclei defines the angle of division relative to the vector defined by the basement membrane. This assay determines division orientation in telophase to analyze division vectors because mitotic spindles at earlier stages of mitosis may not yet have adopted their final orientation. Division angles were measured by at least 2 observers and then angles were binned into 10° increments using Prism 8 and plotted as radial histograms using Origin 2016. For statistical analyses, oriented cell divisions were grouped into three groups: planar ($0 \leq x < 30^\circ$), oblique ($30 \leq x < 60^\circ$), and perpendicular ($60 \leq x < 90^\circ$). Chi-square tests were used for statistical analyses.

Quantification of Ki67⁺, EdU⁺, and pHH3⁺ Cells

Quantification of the frequency of cycling cells (Ki67⁺), mitotic cells (pHH3⁺), and cells in S-phase during the 2 h labeling period (EdU⁺) was determined using FIJI. In Figure S3K, cells that have exited S-phase and entered G2/M during the labeling period are double-labeled with EdU and pHH3 (EdU⁺/pHH3⁺), whereas cells still within S-phase are only EdU⁺. Every DAPI+ basal cell along the entire anterior-posterior axis of the palate was counted in each experimental condition, in multiple slides ($n \geq 2$), and in multiple embryos ($n \geq 3$). Using DAPI+ cells only allowed for measurements to be blinded during each measurement.

Clone Size Quantification from Whole Mounts

For clonal surface volume quantification of 1 month lineage-traced clones (Figure 5A), the endogenous RFP signal from the *Krt14^{CreER}; LSL-Confetti* reporter was tile-scan imaged using a Leica TCS SPE-II 4 confocal with ACS APOCHROMAT 10x/0.30 air objective. Optical section thickness was manually manipulated for thicker slices (10 μm) to preserve fluorescent signal. LAS X stitched image files (.tiff) were uploaded into Imaris v8.4 (Bitplane) and cropped/reoriented. The RFP signal from labeled clones was used to generate statistically coded 3D surfaces using the Imaris “surfaces” feature for the entire image at once.

Quantification of LRIG1 Enrichment

Measurement of enrichment values was performed using FIJI on tile-scanned confocal images acquired at 20x/1.5x optical zoom. Each cell was circumferentially measured for LRIG1 protein fluorescence values using the FIJI freehand line tool (Line Width = 5) on the same magnification for each image. Five random values were also acquired and averaged for LRIG1 expression in the lamina propria, which was defined as the “baseline.” Enrichment was calculated as the circumferential basal epithelial cell fluorescence of each cell divided by the average lamina propria fluorescence for each tissue section. Every DAPI+ basal cell was counted for each experimental condition, in multiple slides ($n \geq 2$), and in multiple embryos ($n \geq 2$).

Statistical Analyses

All statistical analyses, plots, graphs, and radial histograms were generated using Prism 8 (GraphPad) and Origin 2016 (OriginLab). *p* values: * $p < 0.05$, ** $p < 0.01$, *** $p < 0.001$. Categorical values, such as binned division orientation data, were analyzed by chi-square tests. Similar results were observed when Kolmogorov-Smirnov tests were performed on cumulative frequency distributions of division angles (e.g., Figure S1C versus Figure 1B). Continuous data were analyzed by Student's *t* test except where data were not normally distributed, in which case the Mann-Whitney test was applied. For normality tests, Shapiro-Wilk, and D'Agostino-Pearson omnibus tests were used. For bar graphs, error bars represent standard error of the mean (SEM) unless otherwise indicated in the text/figure legends. For box-and-whisker plots, the boxes represent the minimum and maximum values, the horizontal line represents the median, and the “plus” represents the mean. Where “*n*” values are indicated in figure panels, the first value represents the number of samples while the value in parentheses indicates the number of animals from which this was pooled. For stacked bar graphs, each box represents a mean value of assigned category from >3 animals/experiment. For cumulative frequency plots, each line represents >3 animals/experiment.

DATA AND CODE AVAILABILITY

Plotly scripts are deposited on GitHub (<https://github.com/byrdkm/oral-stem>). RNA-seq data are deposited on GEO (Accession number GEO: GSE139146).